

Conditions of loss cone filling by scattering on the curved field lines for 30 keV protons during geomagnetic storm as inferred from numerical trajectory tracing

S. Dubyagin ¹, S. Apatenkov ², E. Gordeev ², N. Ganushkina ^{1,3}, and Y. Zheng ⁴

¹Finnish Meteorological Institute, Helsinki, Finland

²St. Petersburg State University, St. Petersburg, Russia

³Climate and Space Science and Engineering Department, University of Michigan, Ann Arbor, MI, USA

⁴Space Weather Laboratory, Code 674.0, NASA Goddard Space Flight Center, Greenbelt, Maryland, USA

Key Points:

- 30 keV proton trajectories are traced to model the loss cone filling by scattering on the curved field lines during geomagnetic storm
- Critical value of adiabaticity parameter (K_{cr}) corresponding to the loss cone filling varies in the range of 4–8
- This K_{cr} variation is due to variations of the equatorial loss cone size and the guide component of magnetic field in the current sheet

Corresponding author: Stepan Dubyagin, stepan.dubyagin@fmi.fi

This is the author manuscript accepted for publication and has undergone full peer review but has not been through the copyediting, typesetting, pagination and proofreading process, which may lead to differences between this version and the [Version of Record](#). Please cite this article as doi: [10.1029/2020JA028490](https://doi.org/10.1029/2020JA028490).

This article is protected by copyright. All rights reserved.

Abstract

The rate of pitch angle scattering on the curved magnetic field lines is well parameterized by the ratio of the minimum field line curvature radius to the maximum effective particle gyroradius ($K = R_C/r_g$). The critical value of this ratio (K_{cr}) corresponding to the loss cone filling is of special interest since it corresponds to the low altitude isotropic boundaries (IBs). The early theoretical estimates gave $K_{cr} = 8$, whereas recent estimations of the K parameter on the field lines corresponding to the observed IBs during the geomagnetic storms revealed K_{IB} values in the range of 3–30. We numerically trace the trajectories of the 30 keV protons in the magnetic field of the global magnetohydrodynamic simulation of the intense storm in order to infer statistical distribution of K_{cr} . The electric field and effects of non-stationarity are neglected in this study. It is found that although the K_{cr} values do show some variations during the course of the storm, its range is rather narrow $4 < K_{cr} < 8$. The result suggests that higher K_{IB} values found in the observational studies, if not caused by the magnetosphere-ionosphere mapping error, should be attributed to some other mechanism of pitch angle scattering. The K_{cr} values tend to be lower (4–6) during the main phase because the region of low K values approaches the Earth and the equatorial loss cone size becomes larger due to a larger equatorial magnetic field in the near-earth region. The remaining variation of K_{cr} is explained by the presence of the guide component of the magnetic field.

1 Introduction

Two the most debated processes violating the adiabatic ion motion in the night-side magnetosphere which lead to the particle scattering in the atmospheric loss cone are wave-particle interaction (e.g. Kennel & Petschek, 1966) and the scattering on the curved field lines in the magnetotail current sheet (e.g. Büchner & Zelenyi, 1989). Hereafter the latter mechanism will be referred to as *field line curvature* (FLC) scattering. The ion interaction with waves mostly occurs in the inner magnetosphere (e.g. Erlandson & Ukhorskiy, 2001; Yahnin & Yahnina, 2007) whereas the FLC scattering is responsible for isotropic precipitations from the plasma sheet (Sergeev et al., 1993). Hypothetically, these two processes can operate collectively in the transition region between the plasma sheet and the inner magnetosphere and form merged precipitations.

In contrast to the pitch angle scattering due to wave-particle interaction, which depends on multiple parameters in a very complex manner, the amplitude of the FLC scat-

50 tering is well parameterized by the adiabaticity (or curvature) parameter K : the ratio
51 of the minimum curvature radius of the field line to the maximum effective particle gy-
52 roradius calculated for the full particle energy in the current sheet center (Büchner &
53 Zeleny, 1986; Büchner & Zelenyi, 1989). The lower K , the stronger the scattering. Orig-
54 inally, the K parameter was defined for a simple symmetric magnetic field reversal con-
55 figurations with zero guide component. In this paper, we use the K definition general-
56 ized for arbitrary current sheet configurations as $K_{min} = \min(R_C/r_g)$, where the min-
57 imum is found along a given field line and curvature radius is calculated without any as-
58 sumptions about the field line shape. It can be shown that the K_{min} parameter is roughly
59 proportional to the squared magnetic field (Sergeev et al., 1993). For this reason, in the
60 near-Earth region, the K_{min} parameter increases sharply toward the Earth along with
61 the magnetic field magnitude. At some critical point, the FLC scattering becomes too
62 weak to deflect the particle in the atmospheric loss cone and this point corresponds to
63 abrupt drop in the precipitating flux observed on the low-altitude satellites – so called
64 *isotropic boundary* (IB).

65 Since the magnetic field in the equatorial magnetosphere undergoes dramatic vari-
66 ations with geomagnetic activity, the location of the inner boundary of the loss cone fill-
67 ing at the neutral sheet (and IB at low-altitude) also reveal the dynamic variations mov-
68 ing toward the Earth (equatorward) during the magnetic field depression and retreat-
69 ing tailward (poleward) during the recovery. For this reason, and because of availabil-
70 ity and coverage of the low-altitude observations, IBs have been used for long time as
71 a tool of the near-Earth magnetotail remote sensing (West et al., 1978; Sergeev et al.,
72 1993), or as an index of geomagnetic activity (Gvozdevsky & Sergeev, 1996; Asikainen
73 et al., 2010). In addition, analyses of the energetic proton trajectories in the test mag-
74 netic configurations were conducted by several authors to determine the critical value
75 of the K_{min} parameter (K_{cr}) corresponding to the boundary where the scattering am-
76 plitude reaches the size of the loss cone and it becomes fully filled, and so that, corre-
77 sponding to the IBs (Sergeev et al., 1983; Tsyganenko, 1982; Delcourt et al., 1996). For
78 a several test analytical magnetic configurations, the narrow range of $K_{cr} = 6-10$ was
79 found by the authors. This enables one to connect the low-altitude IB observations with
80 characteristics of magnetic configuration of the magnetospheric empirical models and sim-
81 ulations and thus to asses their mapping accuracy (M. V. Kubyshkina et al., 1999; Shevchenko
82 et al., 2010).

83 It should be stressed that all aforementioned IB applications are only possible if
 84 IB are formed by FLC scattering mechanism. However, the wave particle interaction also
 85 can lead to the isotropic precipitation and IB formation. For example, the localized isotropic
 86 precipitations of energetic protons equatorward from the typical IB location were indeed
 87 observed and their connection with ElectroMagnetic Ion Cyclotron (EMIC) waves have
 88 been reliably established (Yahnin & Yahnina, 2007; Popova et al., 2018; Semenova et al.,
 89 2019). Gvozdevsky et al. (1997) studied the slightly anisotropic precipitation of ener-
 90 getic protons adjacent to IB (on equatorward side), apparently related to wave-particle
 91 interaction mechanism operating in the equatorial region. It can be speculated that strength-
 92 ening of this mechanism would lead to IB formation at lower latitudes and mapped to
 93 the higher K_{min} region in the magnetotail. Finally, the condition $K_{cr} = const$ predicts
 94 that IBs for particles with different energies should reveal the energy dispersion with higher
 95 energy IBs located at lower latitudes (due to increase of a particle gyroradius with an
 96 energy increasing). However, the opposite dispersion is often observed (Donovan et al.,
 97 2003; Dubyagin et al., 2013; Sergeev, Chernyaeva, et al., 2015) and can be explained by
 98 the wave-related mechanism of the IB formation (Liang et al., 2014). In contrast to FLC-
 99 scattering, the efficiency of the wave-induced scattering does not depend directly on K_{min}
 100 parameter and there is no reason to believe that this mechanism also produces IB at the
 101 $K_{min} = 6-10$ point.

102 One of the methods to elucidate the occurrences of the IBs formed by FLC and wave
 103 scattering is estimating the K_{min} at the field line corresponding to the observed IBs us-
 104 ing empirical magnetospheric models or magnetohydrodynamic simulations. Hereinafter,
 105 we discriminate two notations: K_{cr} denotes a critical value of K_{min} corresponding to the
 106 loss cone filling by FLC-scattering obtained by numerical tracing of particle trajectories
 107 in the specific magnetic configurations (e.g. Sergeev et al., 1983), and K_{IB} denotes a value
 108 of K_{min} estimated at that field line where the real IB is observed, irrespective of the IB
 109 formation mechanism. The K_{IB} values which are close to the K_{cr} likely correspond to
 110 the FLC-scattering and K_{IB} values which are prominently greater than K_{cr} definitely
 111 correspond to some other mechanism of the pitch angle scattering.

112 Somewhat conflicting results were obtained for quiet-time IB observations: on one
 113 hand, Haiducek et al. (2019a) found that K_{IB} values for 30 keV protons were very close
 114 to K_{cr} ; on the other hand, rather broad statistical distribution of the K_{IB} values ($K_{IB} \approx$
 115 $3-30$) was found by Ilie et al. (2015) and Sergeev, Chernyaev, et al. (2015). The share

116 of the high K_{IB} values is even higher during the geomagnetic storms; Dubyagin et al.
 117 (2018) and Haiducek et al. (2019b) reported that for $\sim 20\%$ – 50% of storm time IBs the
 118 K_{IB} values were greater than 13. Such K_{IB} values apparently cannot be explained by
 119 FLC-scattering. These are not totally unexpected results because the occurrence of in-
 120 tense EMIC waves, which are capable of scattering the energetic protons into the loss
 121 cone, peaks during the geomagnetic storms (Halford et al., 2010; Keika et al., 2013; Us-
 122 anova et al., 2012; Chen et al., 2019). On the other hand, the accuracy of the K_{IB} es-
 123 timation is very difficult to assess and possibility that the broad distribution is a result
 124 of error in magnetosphere-ionosphere mapping or error of K_{min} estimation cannot be
 125 absolutely ruled out. In addition, the numerical values of K_{cr} were obtained for a lim-
 126 ited number of relatively simple analytical current sheet configurations: the parabolic
 127 and Harris current sheets as well as the current sheet of T89 magnetospheric model. At
 128 the same time, it was shown that there can be significant deviations from these K_{cr} val-
 129 ues for more complex current sheet configurations (Delcourt et al., 2000, 2006). It is known
 130 that during a geomagnetic storm thin current sheet can develop at distances as close as
 131 $r \approx 5R_E$ or even closer (Tsyganenko & Sitnov, 2005, 2007). At this distance, the mag-
 132 netic configuration at the IB formation region can not be considered as one-dimensional
 133 and the near-Earth current can be bifurcated into horn-like configuration (Tsyganenko
 134 & Andreeva, 2017). For this reason, the range of K_{cr} -values obtained previously for the
 135 simple magnetic configurations might not be applicable for such configurations.

136 The purpose of this paper is to statistically examine the condition of the loss cone
 137 filling by FLC scattering mechanism for a variety of current sheet configurations dur-
 138 ing intense geomagnetic storms. We performed numerical tracing of 30 keV proton tra-
 139 jectories in the magnetic field of MHD simulation of the intense storm event. The MHD
 140 representation of magnetic configuration is self-consistent with the isotropic plasma pres-
 141 sure and even if the actual configuration of the magnetosphere might be different, we ex-
 142 pect that physics-based modeling results in a realistic configuration (Gordeev et al., 2015).
 143 The energy of 30 keV was chosen because it is covered by the majority of proton detec-
 144 tors on low-altitude satellites used for IB observations. 30 keV protons distributed over
 145 the loss cone were traced backward in time and their origin with respect to the loss cone
 146 in the opposite hemisphere was determined. Analyzing the percentage of the particles
 147 whose origins were outside the loss cone, we can determine the degree of loss cone fill-
 148 ing. The particles were launched at different latitudes for seven MLT sectors covering

149 the nightside during sudden commencement, main phase, early recovery phase with 1 h
 150 cadence. For each latitudinal profile, we determined the latitude where the loss cone be-
 151 came fully filled and calculated the K_{cr} -parameter on the corresponding field line. We
 152 present the statistical distribution of the K_{cr} -parameter and analyze the conditions in
 153 the field reversal region responsible for its variation. Possible effects related to the elec-
 154 tric field or non-stationary magnetic configuration are ignored in this study.

155 2 MHD Simulation of the Storm 22–26 June 2015

156 The intense geomagnetic storms occurred on 22–23 June 2015 with the Dst index
 157 reaching minimum of -204 nT on 04 UT, 23 June. There were three storm intensifica-
 158 tions, but in this paper we will focus only on the first two which occurred during 1.5 day
 159 interval 22 June, 12 UT – 24 June, 00 UT. Figure 1a shows the variation of the SYM-
 160 H index during this period (SYM-H and solar wind variations for the entire storm pe-
 161 riod can be found in M. Kubyshkina et al. (2019)). The entire event was simulated by
 162 Space Weather Modeling Framework (SWMF) MHD model (Block Adaptive Tree So-
 163 lar Wind-Roe-Upwind Scheme with Rice Convection Model (Tóth et al., 2005)) via the
 164 Community Coordinated Modeling Center’s Runs-on-Request service with the running
 165 ID Yihua_Zheng_080416_2 run.

166 The near-Earth magnetosphere was well covered by the magnetic field observations
 167 on board six missions. M. Kubyshkina et al. (2019) compared these magnetic field ob-
 168 servations to the SWMF output and found a remarkable agreement with the average er-
 169 ror being within ~ 20 nT with only ~ 4 h period around 20 UT on June 22 when the er-
 170 ror reached ~ 60 nT; very good result for modeling such an intense storm. Though the
 171 error was large during the SYM-H drop at ~ 20 UT on June 22, the agreement with ob-
 172 servations for the particular moment is not critical for our study. Indeed, since the sim-
 173 ulations obeys physical MHD equations, the SWMF configuration is expected to be re-
 174 alistic and physically-consistent. The simulation spatial grid resolution is $0.25R_E$ inside
 175 $|X|, |Y|, |Z| < 8R_E$ cube and $0.5R_E$ outside that region. Since we are especially inter-
 176 ested in the storm peak configurations when the thin current sheet approaches the Earth,
 177 we expect that the IB formation region will be inside the fine resolution region.

178 First, we use SWMF simulation to analyze how the distribution of the K -parameter
 179 changed during the course of the storm for different MLTs. For this purpose, the K -parameter

Author Manuscript

180 for 30keV protons was calculated on the meridional planes for seven nightside MLT sec-
 181 tors with 1h temporal resolution. Since the MLT slices do not necessarily cross the sim-
 182 ulation grid nodes, trilinear interpolation of the magnetic field vector components was
 183 used to calculate magnetic field between the grid nodes. The finite difference method
 184 was used for curvature radius estimation. Note also that although K was estimated on
 185 the meridional plane, it was calculated for the full 3D SWMF magnetic field and finite
 186 differences were calculated for all three directions. Since we are especially interested in
 187 the location of the region where IB is presumably formed, for every MLT slice, we find
 188 the earthward edge of $K \leq 8$ region. Figure 1b shows the result as time-MLT distri-
 189 bution. The radial distance to the closest (to the Earth) $K = 8$ point is color coded
 190 and also shown as a number in each time-MLT bin. It can be seen that the region with
 191 $K \leq 8$ comes to the Earth as close as $r = 4.7R_E$ during the main phase of the storm.
 192 There is also a moderate MLT asymmetry with low K region coming closer to the Earth
 193 at the dusk-midnight MLT sector. It can be also seen that some time-MLT bins are left
 194 blank. It is because we limited our search by $r = 12R_E$. Thus, the blank bins at 19 UT
 195 on June 22, during sudden commencement and following SYM-H drop, indicate that the
 196 $K \leq 8$ region moved outward ($r > 12R_E$) for MLT=22–00 MLT sector. It can be in-
 197 terpreted as a localized dipolarization. The thick current sheet also often forms at the
 198 flank MLT sectors and results in the blank bins at MLT= 18, MLT= 06.

199 For three time-MLT slices, we show the distribution of K -parameter in the merid-
 200 ional plane in Figure 2. Time and MLT are shown at the top of the figures. Three pan-
 201 els correspond to (a) pre-storm period, (b) SYM-H minimum, and (c) early recovery phase.
 202 The blue region roughly corresponds to $K \leq 10$. It can be seen that in Figure 2b (cor-
 203 responding to June 22, 22 UT, MLT=22) this region is much thinner and located much
 204 closer to the Earth in comparison to Figures 2a, c. This can be considered as an indi-
 205 cation of the thin intense current sheet formation but it should be remembered that there
 206 is no one-to-one correspondence between K and current density. Although this plot cor-
 207 responds to the moment just after the SYM-H first minimum, it should be noted that
 208 the storm phase timing can be different in MHD simulation. Three white asterisks show
 209 the earthward edges of the regions of $K \leq 20$, $K \leq 8$, $K \leq 3$. Note that in Figure 2a,
 210 there are no $K \leq 3$ points inside $r = 12R_E$. Finally, it should be noted that the K
 211 estimate shown here is not very accurate due to trilinear interpolation of the field com-
 212 ponents and we use it as a first approximation.

Figure 2. Examples of the K -parameter distribution in the meridional plane for (a) pre-storm, (b) SYM-H minimum, and (c) early recovery phase.

3 Analytical Approximation of the Simulation Magnetic Field

To trace particle trajectories we need a physically consistent continuous and relatively smooth analytical approximation of the SWMF simulation magnetic field. It is convenient to use some magnetic potentials because this method provides divergence free magnetic field. We introduce additional simplification assuming that magnetic configuration possesses axial symmetry in SM coordinate system. We use Euler potentials (e.g. Stern, 1966) to describe magnetic field vector in meridional plane of SM system:

$$B = [\nabla\alpha \times \nabla\beta] \quad (1)$$

where α is a function of two cylindrical coordinates $\rho = (x^2 + y^2)^{\frac{1}{2}}$ and z , and $\beta = \varphi$ (azimuthal angle). In this case, for ρ and z components of magnetic field in cylindrical SM coordinates we get:

$$B_\rho = -\frac{1}{\rho} \frac{\partial\alpha}{\partial z} \quad (2)$$

$$B_z = \frac{1}{\rho} \frac{\partial\alpha}{\partial\rho} \quad (3)$$

Alpha is represented as a polynomial expansion:

$$\alpha(\rho, z) = \sum_{i=0}^n \sum_{j=0}^m C_{ij} \rho^i z^j \quad (4)$$

As a result, the field components depend on C_{ij} coefficients linearly and the magnetic field vectors can be fitted using usual least squares method.

Since for the axially symmetric configurations with $\partial B_\varphi / \partial \varphi = 0$ the magnetic field is divergence free for arbitrary $B_\varphi(\rho, z)$ distribution, there is no need to use any magnetic potential. We can use polynomial expansion directly for the B_φ component:

$$B_\varphi(\rho, z) = \sum_{i=0}^n \sum_{j=0}^m A_{ij} \rho^i z^j \quad (5)$$

Since we need the accurate magnetic field model only in the region where the particles undergo moderate pitch angle scattering, that is, $K = 3-20$, we developed automatic algorithm selecting the region on the meridional plane where the field is approximated. The example of this region selection can be seen in Figure 3a (shown by the blue curves). To select this region, we used the points shown as white asterisks in Figure 2 (these points correspond to $K = 3, 8, 20$ in the current sheet center). The outer boundary was located $1R_E$ outward from the $K = 3$ point. For those events when there were no $K \leq 3$ points inside $r = 12R_E$, the outer boundary was set $2R_E$ outward from the $K \leq 8$ edge. In all cases, the outer boundary was set not further than $r = 12R_E$. The inner boundary was set on a sphere with $r = 3.3R_E$. The top and bottom boundaries were constructed as a combination of straight and dipole lines such that there was at least $0.5R_E$ margin between the boundary and the field line corresponding to $K = 3$ point. Our analytic model (Equations 2-5) was fit to the SWMF magnetic field vectors on a meridional plane inside this region. It should be noted that Equations 2, 3, and 5 describe only external magnetic field of SWMF simulation with the dipole field subtracted. To give more weight to the points at low K region (low B regions), we minimized a mean relative error $Err = \Delta B / B$, where ΔB is a difference between the SWMF and the analytical model vectors, and B in the denominator is the full SWMF field magnitude (including dipole).

To keep the number of terms in expansions for Euler potential and B_φ within reasonable limit and to avoid Runge's phenomenon (oscillation at the edges of an approx-

Figure 3. (a) Example of the field lines (red) traced from the starting points (blue crosses in the left part). The green asterisks near the field line apexes mark the location on K_{min} . Blue contour shows the boundary of the analytical approximation of the MHD simulation field. (b) The tracing configuration is explained.

259 imated interval that occurs when using polynomials of high degree), we elaborated the
 260 following strategy. First, we tried all combinations of the highest powers $1 \leq n \leq 8$
 261 and $1 \leq m \leq 8$ and analyzed how the error of the approximations behaved. We plot-
 262 ted Err versus the total number of terms in these expansions ($N = n \cdot m$). It was no-
 263 ticed that Err for the Euler potential first decreased fast with N increasing but then it
 264 reached some level and did not reveal further significant decrease. On the contrary, the
 265 error for B_φ expansion revealed stable decrease with N increasing. It can be understood
 266 taking into account that we approximated 3D configuration by divergence free axially
 267 symmetric field. At some level of detalization, the divergence free approximation just
 268 can not reproduce B_ρ and B_z distribution which is not divergence free because in 3D con-
 269 figuration zero divergence is ensured also by a variation in azimuthal direction ($\partial B_\varphi / \partial \varphi \neq$
 270 0). To select the optimal values of n, m for the Euler potential fit, two reference values
 271 of the relative error are defined: Err_0 is the mean relative error when the SWMF mag-
 272 netic field is approximated by its mean value, and Err_{min} is the minimum mean rela-
 273 tive error over all possible combinations of $n < 8$ and $m < 8$. The optimal combina-
 274 tion of n and m was defined in such a way that it gives minimum number of terms in
 275 the expansion and at the same time satisfies a condition $Err(n, m) \leq Err_{min} + (Err_0 -$
 276 $Err_{min}) / 100$ (the error for the optimal n, m differs from Err_{min} less than 1% of differ-
 277 ence between Err_0 and Err_{min}). For the B_φ fit, we used similar strategy for definition
 278 of optimal n, m but the requirement was simpler: minimal $N = n \cdot m$ for $Err(n, m) \leq$
 279 0.01 . For the majority of configurations the n and m do not exceed value of 6. Two sets
 280 of the magnetic field expansion coefficients $C_{i,j}, A_{i,j}$, corresponding to the optimal n, m
 281 values for the Euler potential and B_φ approximations, were obtained for every time step
 282 and MLT sector. These coefficients represent the local axially-symmetric analytical model-
 283 approximation of the SWMF field.

284 To asses the accuracy of our analytical model, we plot relative error of the SWMF
 285 magnetic field representation in Figure 4a. The error is computed for the full field (ex-
 286 ternal sources plus dipole) and shown versus time and MLT. The numbers duplicate the
 287 color representation. The median error is computed only for the region where the scat-
 288 tering take place $2 \leq K \leq 12$. It can be seen that the error is lowest during the main
 289 phase. It is due to smaller size of the region which should be modeled. Indeed, during
 290 the main phase $3 < K_{min} < 20$ region approaches the Earth (see the white points in
 291 Figure 2b), and the region where the field should be approximated becomes very small.

292 On the other hand, the median errors can be as large as $\sim 20\%$ during the recovery phase.
 293 In Figure 4b, we show the relative error of the K parameter estimated from our analyt-
 294 ical model. It generally reveals the variation similar to the magnetic field error but with
 295 somewhat larger values. Note that although the median relative error of 20% for some
 296 configurations seems to be very large, it usually corresponds to an absolute error $\Delta K \sim$
 297 1–2 (see Figure S2 in Supporting Information).

298 4 Methodology

299 To model the loss cone filling as a function of K , we trace the trajectories of the
 300 particles with the initial velocity vectors inside the loss cone from a set of points above
 301 the ionosphere distributed in latitude and corresponding to different minimum K val-
 302 ues at the magnetospheric part of the field line (K_{min}). To determine the correspondence
 303 between the latitudes and K_{min} values, the field lines should be traced from the start-
 304 ing points and K parameter should be calculated along the field lines. In addition, the
 305 size of the loss cone should be evaluated from the magnetic field magnitude at the op-
 306 posite hemisphere. After the loss cone size is defined, the initial vectors of the particle
 307 velocities inside the loss cone can be set and the trajectory tracing can be initiated. Thus,
 308 the sets of the spatial starting points with corresponding K_{min} values and the loss cone
 309 sizes should be defined for all desired MLT sectors and times.

310 4.1 Spatial starting points

311 One of advantages of using Euler potential is simplicity and accuracy of the field
 312 line tracing because α is constant on a given field line. For every magnetic configuration,
 313 represented by its analytical model, we traced the magnetic field lines outward from the
 314 sphere $r = 3.5R_E$ (slightly above the inner boundary of the analytical model) via the
 315 equator and then to the sphere of the same radius in the opposite hemisphere. Figure 3b
 316 shows schematically the geometry. The field line is traced from the starting point in the
 317 northern hemisphere (st1) to the point in the southern hemisphere (st2). The K -parameter
 318 was calculated along the field line and a minimum value for a given field line was deter-
 319 mined. Note, that in contrast to the K -parameter shown in Figures 1 and 2, which was
 320 calculated from the linearly interpolated SWMF magnetic field, this time the K -parameter
 321 is calculated using the smooth analytical model. Note that B_φ component was not ig-
 322 nored and also was used for the K calculation. The field line starting points were dis-

Author Manuscript

323 tributed in latitude to cover $3 \leq K_{min} \leq 20$ region and the latitudinal increment was
 324 selected to keep the increment in K_{min} of ~ 1 .

325 The loss cone size of the downgoing particles at the point st1 depends on the mag-
 326 netic field magnitude in the opposite hemisphere at the altitude where the particles are
 327 lost due to collisions with the atmospheric particles (i2 point). Note that this loss cone
 328 definition differs from the traditional one which defines the loss cone size by the iono-
 329 spheric magnetic field in the same hemisphere (i1 point). The altitude of the loss cone
 330 formation varies due to the atmosphere density variations but we use 120 km as a ref-
 331 erence altitude of the loss cone formation in this study. Since our analytical model is de-
 332 fined only for the altitudes above $r = 3.5R_E$, we can not use it for the field line trac-
 333 ing between st2 and i2 points. Instead, we trace the field lines between $r = 2.5-3.5R_E$
 334 using trilinear interpolation of the MHD field, and below $r = 2.5R_E$, we use analyti-
 335 cal equation for the dipole field line to project the points to the Earth's surface where
 336 a magnetic latitude of the point is calculated. Since the simulation uses a dipole repre-
 337 sentation of the Earth's field, this magnetic latitude can be interpreted as a *Altitude Ad-*
 338 *justed Corrected Geomagnetic* (AACGM) latitude.

339 The magnitude of the Earth's magnetic field at the ionospheric altitude depends
 340 both on the latitude and on the longitude. Figure 5 shows the magnitude of the IGRF
 341 model magnetic field at 120 km altitude versus AACGM latitude for two hemispheres.
 342 The upper and lower curves of the same color show the range of the longitudinal vari-
 343 ation of the magnetic field for a given latitude. It can be seen that for the southern hemi-
 344 sphere, for the latitudes less than 60° , a longitudinal variation of the magnetic field can
 345 result in two times difference of the magnetic field magnitudes corresponding to the same
 346 AACGM latitude: manifestation of the South Atlantic Anomaly. Since the SWMF sim-
 347 ulation lacks the longitudinal dependence of the Earth's field as well as to generalize our
 348 results to arbitrary longitudes and times, we use two extreme values of ionospheric mag-
 349 netic field (upper and lower curves in Figure 5) for calculation of the loss cone size and
 350 the corresponding results will be designated by *Bi_min* and *Bi_max* suffixes.

351 We use the 5th-degree polynomial fits to the curves in Figure 5 to calculate the loss
 352 cone size for the AACGM latitude of the given magnetic field line. The analysis of the
 353 loss cone filling have been done for all four curves in Figure 5, but intermediate results

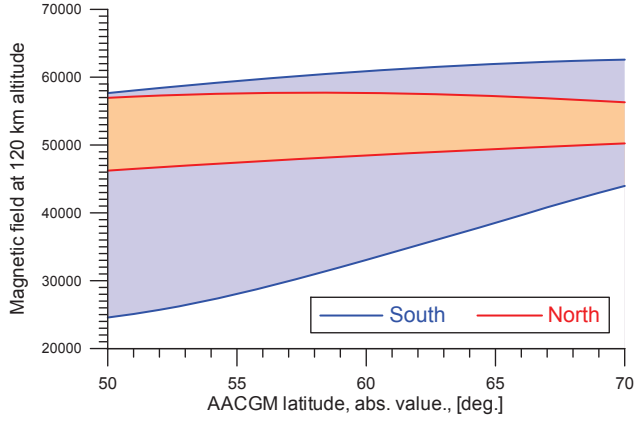


Figure 5. IGRF magnetic field at 120 km altitude versus absolute value of AACGM latitude. The filled areas between the red and blue curves show the span of the longitudinal variation for northern and southern hemispheres, respectively.

are shown only for the loss cone size estimated from the minimum magnetic field magnitude in the southern hemisphere (lowest curve in Figure 5).

4.2 Initial distribution in the velocity space

For a given kinetic energy ($E = 30\text{keV}$ is considered in this study), the magnetic moment corresponding to the loss cone edge (μ_{LC}) can be calculated as $\mu_{\text{LC}} = E/B_{i2}$. Thus, for the st1 point, the edge of the loss cone in the velocity space can be calculated as:

$$v_{\perp\text{LC}}^2 = \frac{2E}{m} \frac{B_{\text{st1}}}{B_{i2}} \quad (6)$$

After the loss cone size is determined, we set initial distributions of particle velocities in the velocity space: 372 points evenly distributed in $v_{\perp 1}, v_{\perp 2}$ plane inside the loss cone (see Figure 6). It should be noted that the magnetic moment conserves only in the frame moving with the guiding center (Stephens et al., 2017). The guiding center drift velocity is negligible at the ionospheric altitude but it cannot be neglected at $r = 3.5R_E$. For this reason, the velocity in the left part of Equation 6 is given for a drifting frame, and it should be converted to a stationary frame by addition of the drift velocity vector. The drift velocity vector was calculated using standard expressions for the gradi-

ent and curvature drifts (Baumjohann & Treumann, 1996) and finite difference for the magnetic field gradient and curvature radius estimation.

4.3 Numerical methods and accuracy control

The particles were traced using 4th order Runge-Kutta-Nyström method (see e.g. Bock & Krischer, 1998). The method was used with a variable step-size computed for each new time-step as

$$\Delta t = \frac{(\Delta\alpha \cdot g)^{\frac{1}{4}}}{B}, \quad (7)$$

where B is the magnitude of magnetic field at the previous time-step, $\Delta\alpha$ is the allowed error in pitch angle at the ending point of a trajectory, and g is the constant calculated for each spatial starting point as described in Supporting Information S1 (the derivation of Equation 7 can be also found there). $\Delta\alpha$ is set to 1/200 of the loss cone size at the ending point. We have tested this step-size selection procedure performing backward in time and then forward in time tracings for several starting points and comparing initial and final pitch angles. For all tested trajectories the resulting error in pitch angle was at least ten times smaller than the allowed error $\Delta\alpha$.

4.4 Trajectory classification

For every time and MLT sector, we organize the tracing procedure as two embedded loops: one loop is over the spatial points (blue crosses at the left part of Figure 3a), and another one is for the velocity vectors inside the loss cone (evenly distributed points in Figure 6). There is a class of orbits for which the particle can be trapped near the current sheet for prolonged time (Speiser, 1965; Kaufmann & Lu, 1993; Larson & Kaufmann, 1996), for this reason we limit the time of tracing as double time needed for particle with zero pitch angle to reach the opposite hemisphere. Even at $r = 3.5R_E$, the loss cone size is still rather small ($< 10^\circ$), so the time required for the particle to reach the opposite hemisphere if no strong pitch angle scattering has occurred can be evaluated as L/v , where L is the length of the field line between st1 and st2 points (see Figure 3b), and v is the full particle velocity. Thus, the limit for the tracing time is $t_{lim} = 2L/v$.

Eventually, we trace the particle trajectories backward in time and tracing is stopped when one of the following conditions is met:

1. The particle reaches $r = 3.5R_E$ sphere in the opposite hemisphere
2. The particle returns back to $r = 3.5R_E$ in the same hemisphere (it is reflected from the minimum K region).
3. The particle crosses the outer boundaries of the magnetic field model applicability region (upper, lower, right blue lines in Figure 3a).
4. $t_{lim} = 2L/v$ time is exceeded

For the vast majority of the trajectories, the first condition is met. In this case, the resulting particle velocity is converted to the drifting frame and the magnetic moment is calculated. The moment is compared to μ_{LC} , corresponding to the loss cone edge, to check whether the particle is still inside the loss cone or outside it. The latter result corresponds to the particle scattered into the loss cone during its crossing of the field reversal, while former results indicates that there is no particle at this point of the velocity space since there are no energetic particles going upward from the atmosphere. The conditions 2–4 correspond to the relatively strong pitch angle scattering, and although there is an uncertainty about the particle origin (because both options are possible after several crossing of the field reversal), these trajectories are marked as originated outside the loss cone.

5 Results

Figure 6 shows the initial distribution of the perpendicular velocities over the loss cone ($v_{\perp 1}, v_{\perp 2}$ normalized by perpendicular velocity corresponding to the loss cone edge) for the spatial points corresponding to different K_{min} values (shown at the top of each panel). The blue crosses and red triangles correspond to the trajectories which are originated in the loss cone and outside the loss cone, respectively. It can be seen that for $K_{min} = 8.6$ (Figure 6a), the scattering is weak and all trajectories originate in the loss cone. In reality, this would correspond to the empty loss cone. For lower K_{min} (Figure 6b), more than half of the loss cone is filled (the trajectories originate outside the loss cone, red triangles). Note, that the loss cone filling depends on the gyro-phase. It is consistent with the Delcourt et al. (1995) results who showed that the amplitude of scattering depends on the gyration-phase of the particle when it enters the low K region. It should be noted that this gyrophase dependence of the loss cone filling can not be observed at low alti-

Figure 6. Distribution of the initial perpendicular velocities over the loss cone marked according to their origin outside (red) or inside (blue) of the opposite hemisphere loss cone. Three panels correspond to three values of K_{min} (shown at the top left corner of the panel).

430 tudes (e.g. 850 km; altitude of NOAA/POES satellites), because the difference in the
 431 number of gyrations for different pitch angles inside the loss cone becomes too large. Fi-
 432 nally, at $K_{min} = 4.2$ (Figure 6c), whole loss cone is filled (all trajectories have their ori-
 433 gins outside the loss cone).

434 Figure 7 demonstrates the process of the loss cone filling as a function of K_{min} at
 435 higher resolution. Figure 7a show the percentage of the loss cone area filled, calculated
 436 as a ratio of the velocity distribution points originated outside the loss cone to the to-
 437 tal number of points. It can be seen that the loss cone filling starts at $K_{min} \approx 10$ and
 438 the loss cone becomes fully filled at $K_{min} = 4.2$. In Figure 7b, we show the process of
 439 the loss cone filling for different pitch angles. Since the points of velocity distribution
 440 in Figure 6 are organized in circles corresponding to certain pitch angle values, it is easy
 441 to calculate a percentage of the points originated outside the loss cone separately for each
 442 pitch angle. The vertical axis of Figure 7b shows the pitch angle normalized by the loss
 443 cone size (1 corresponds to the loss cone edge). Color shows percentage of the loss cone
 444 area filled for the corresponding pitch angle. Red color corresponds to 100% filling. It
 445 can be seen that loss cone filling starts from its edge at $K_{min} \approx 10$, and gradually prop-
 446 agates to the center at $K_{min} \approx 5$.

Figure 7. Diagrams showing the loss cone filling versus K_{min} -parameter. (a) Percentage of the loss cone area filled. (b) Color shows percentage of the loss cone filled for given pitch angle (normalized by loss cone size).

447 Since the goal of this study is to explain the diversity of the K values estimated
 448 for the observed isotropic boundaries, we need to develop a definition of an isotropic bound-
 449 ary for the output of our trajectory computations, and this definition should be consis-
 450 tent with that for observations. Although the isotropic boundaries can be observed even
 451 on high-altitude missions (Ganushkina et al., 2005), the most studies addressing this topic
 452 have been conducted using the observations of the NOAA/POES satellites at ~ 850 km
 453 altitude (Sergeev et al., 1993; Sergeev, Chernyaeva, et al., 2015). These satellites are equipped
 454 with a suit of the solid state telescopes (Evans & Greer, 2004) pointing in the perpen-
 455 dicular directions one of which (referred to as 0° telescope) is directed radially upward
 456 and detects the fluxes of particles precipitating in the loss cone. Another one (referred
 457 to as 90° telescope), measures the fluxes of the locally trapped particles. At this altitude,
 458 the half-width of the loss cone varies between $45\text{--}90^\circ$, and 30° -aperture of the NOAA/POES
 459 telescope fits reliably inside the loss cone. On the other hand, the telescope can not see
 460 the outer part of the loss cone. In observations, the isotropic boundary is defined as the
 461 most equatorial point where the fluxes are isotropic, that is, the fluxes detected by 0°
 462 and 90° telescopes are equal (withing the accuracy of measurements). Therefore, we de-
 463 fine the isotropic boundary as a first point (moving from high to low K_{min} values) where
 464 the central 1/3 of the loss cone is 100% filled. This criterion typically corresponds to the
 465 filling of the more than 80% of the loss cone area (see Figure S3 in Supporting Informa-
 466 tion). However, since our discretization of the K_{min} values is rather coarse (the differ-
 467 ence between the adjacent K_{min} values can be as large as ~ 1), we consider this K_{min}
 468 value as a lower estimate of the true K_{cr} and we also use the next higher K_{min} value
 469 as an upper estimate for K_{cr} . The corresponding K_{min} values are referred to as K_{cr}^{low}
 470 and K_{cr}^{up} , respectively.

471 Figure 8a shows the color-coded K_{cr}^{low} versus time and MLT . The pairs of num-
 472 bers in the bins show K_{IB} and its upper estimate (next higher K_{min} value). It can be
 473 seen that K_{cr}^{low} does not exceed value of 7 and K_{cr}^{up} does not exceed value of 8. It can
 474 be noticed that somewhat more bins are left blank in comparison to Figure 1. This is
 475 because the algorithm cannot detect IB within the region of the magnetic field model
 476 validity; the values of K_{min} low enough to fill the loss cone are outside $r = 12R_E$. It
 477 should be noted that these configurations are not necessarily correspond to the dipolar-
 478 ized current sheet. They often look as a plateau-like region at $K_{min} = 5\text{--}6$ level.

Author Manuscript

Figure 9. Parameters of the magnetic configuration at $K_{min} = 6$ point versus radial distance: (a) field line curvature radius, (b) magnetic field magnitude.

479 It is apparent from Figure 8 that there is a prominent variation of K_{cr} during the
 480 course of the storm: it is lower during the main phase of the storm especially at the pre-
 481 midnight sector where K_{cr}^{low} can be as low as ~ 4 . Note that it is roughly the same time
 482 and MLT sector when and where the region of the low K values approaches the Earth
 483 (see Figure 1b). This similarity is not just a coincidence. We analyzed the radial pro-
 484 files of the K_{min} parameter and for each profile we identified the point where $K_{min} =$
 485 6. In Figure 9, we show the magnetic field line curvature radius (a) and equatorial mag-
 486 netic field magnitude (b) at $K_{min} = 6$ point versus radial distance. Each symbol cor-
 487 responds to the individual K_{min} radial profile. It can be seen that the closer to the Earth
 488 the point $K_{min} = 6$ is, the lower curvature radius corresponds to this K_{min} value. Since
 489 the gyroradius must follow the curvature radius to keep K_{min} constant and it depends
 490 inversely on magnetic field magnitude, the magnetic field is higher in the near-Earth re-
 491 gion. In turn, higher equatorial magnetic field means larger loss cone size at the equa-
 492 tor since it is expressed as $\alpha_{LC} = \arcsin \sqrt{B_{eq}/B_i}$ (here, B_i is magnetic field in the iono-
 493 sphere). Hence, stronger scattering is needed to fill the larger loss cone and, therefore,
 494 the isotropic boundary is formed at the lower K_{min} values in the near-Earth region dur-
 495 ing the main phase.

Figure 10. K_{cr} versus the loss cone size at the field reversal for the particles traced from (a) northern hemisphere, (b) southern hemisphere. The vertical error bars show the range between the K_{cr}^{low} and K_{cr}^{up} . Color corresponds to the normalized B_φ component.

496 However, K_{min} is not the only parameter controlling the strength of the pitch an-
 497 gle scattering in the field reversal region. In Figure 10, we show K_{cr} versus the equato-
 498 rial loss cone size. The vertical error bars show the range between lower and upper es-
 499 timates of K_{cr} . Figures 10a and 10b correspond to the results obtained for particles
 500 traced from the northern and southern hemispheres, respectively. Although K_{cr} does dis-
 501 play dependence on the loss cone size, the lowest values of K_{cr}^{low} are found for the mid-
 502 range values of the loss cone size. It was shown in a few studies that the guide-component
 503 of magnetic field at the field reversal region affects the intensity of the pitch angle scat-
 504 tering (Büchner & Zelenyi, 1991; Zhu & Parks, 1993; Delcourt et al., 2000). We use the
 505 color palette to show the azimuthal component of the magnetic field (B_φ) normalized
 506 by the full magnetic field magnitude. It can be seen in Figure 10a that lowest K_{cr}^{low} val-
 507 ues correspond to the strong negative B_φ , and more generally, bright blue and red er-
 508 ror bars are located near the lower and upper envelopes of the data point cloud, respec-
 509 tively. The opposite dependence on B_φ can be seen in Figure 10b. Such interhemispheric
 510 asymmetry is in a full agreement with findings of Delcourt et al. (2000), who found that
 511 the pitch angle scattering strengthens or weakens depending on the mutual relationship
 512 between the directions of the particle propagation (and gyration) and the sign of the guide-
 513 component at the field reversal. Note that the spread of the K_{cr} scatter due to B_φ vari-
 514 ation is comparable to the range of variation caused by the variation of the loss cone size.

515 Figure 11 shows the histograms of K_{cr}^{low} (black) and iK_{cr}^{up} (red) for all times and
 516 MLT bins. Figures 11a and 11b are obtained using different models of the loss cone size
 517 dependence on AACGM latitude. The minimum value of the ionospheric magnetic field
 518 (lower blue curve in Figure 5) is used for Figure 11a and maximum value (upper blue
 519 curve in Figure 5) for Figure 11b. Since the loss cone size depends inversely on the iono-
 520 spheric field magnitude, it is not surprising that the histograms in Figure 11b are shifted
 521 towards higher K_{cr} values. However, for both models of the ionospheric field, the val-
 522 ues of K_{cr}^{low} does not exceed value of 7 and K_{cr}^{up} does not exceed value of 8. The peaks
 523 of the histograms are located between $K_{cr} = 6-7$. It is only a bit smaller than $K_{cr} =$
 524 8 value, which is conventionally used in the studies where the isotropic boundaries are
 525 analyzed (e.g. Shevchenko et al., 2010).

Figure 11. Histograms of K_{cr}^{low} (black) and K_{cr}^{up} (red). Panels a and b correspond to the results obtained using the minimum and maximum values of the ionospheric field, respectively. Particles were launched from the northern hemisphere.

6 Discussion

In this paper, we modelled numerically the loss cone filling by 30 keV protons due to FLC scattering during the intense magnetospheric storm. The magnetic configuration was represented by the SWMF simulation. It was found that even the extreme configurations do not lead to significant changes of the loss cone filling conditions: the K_{cr} values do not exceed the value of 8. In fact, the K_{cr} values tend to be lower ($K_{cr} \approx 4$ –6) during the main phase of the storm, when the $K_{min} < 8$ region can approach the Earth as close as $r \approx 5R_E$, and higher ($K_{cr} \approx 6$ –8) during the pre-storm interval and recovery. Although our results seem to indicate that all K_{IB} values greater than 8, found from the observations by Dubyagin et al. (2018) and Haiducek et al. (2019b), can be attributed to wave-particle interaction, yet, there is room for doubts. Our modelling has a number of serious limitations. The main limitation is that we fully neglect the electric field. The large scale electric field inside $L = 6$ can be as strong as 1.5–4 mV/m (e.g. Rowland & Wygant, 1998; Nishimura et al., 2006). Such field can significantly accelerate a proton even during single current sheet crossing. The analysis of the effects related to the electric field is left for the future study. On the practical side, it is con-

542 ceivable that the periods with fast flows in the equatorial region manifest themselves specif-
 543 ically in the low-altitude observations and the corresponding IBs can be discarded or treated
 544 accordingly. This topic certainly deserves further investigation.

545 One more drawback of our approach is that we use axially-symmetric local approx-
 546 imation of the SWMF field instead of 3D-interpolation between the simulation grid nodes.
 547 Figure 4a shows that the median error of our approximation can be as large as $\sim 20\%$.
 548 In addition, the polynomial approximation with a moderate number of terms partly smooths
 549 the smallest-scale structures of the SWMF field. On the other hand, the advantage of
 550 our approach is that it provides divergence-free field which is fast to compute and the
 551 axially-symmetric configuration simplifies the analysis (e.g. calculation of the guide field).
 552 At the very least, our approximation adequately describes the large-scale configuration
 553 in the near-Earth region with strong radial magnetic field gradient.

554 There are also a couple of minor effects which were also ignored. (1) An effect of
 555 the non-stationary configuration on the K_{cr} values is probably insignificant since it takes
 556 only 5 sec for 30 keV proton to cross $2 R_E$ distance (estimate for field reversal region
 557 size) and less than 30 sec to reach the ionosphere. (2) The K_{cr} values depend on the IB
 558 definition. All our results are obtained for IBs defined as the point where central one third
 559 of the loss cone is 100% filled. We also tested a few other definitions and concluded that
 560 reasonable IB definitions do not lead to significant difference in K_{cr} .

561 On the other hand, there is still possibility that at least some fraction of IBs with
 562 large K_{IB} values found by Dubyagin et al. (2018) and Haiducek et al. (2019b) is accounted
 563 for by the errors of ionosphere-magnetosphere mapping and the K parameter estima-
 564 tion. It should be noted that in both studies, special efforts were undertaken to control
 565 the accuracy of the K estimation and mapping. The in-situ magnetic field measurements
 566 in the region of expected IB formation were compared with the model magnetic field and
 567 the correction was applied taking into account the difference between the model and ob-
 568 servations. However, the corrections were based on a number of assumptions, e.g. lin-
 569 ear dependence of estimated $\log K_{min}$ on B_Z error. It was also assumed that the mag-
 570 netic field at the spacecraft location and at the point of true IB formation vary in a co-
 571 herent manner (correlate with each other). In addition, Haiducek et al. (2019a) demon-
 572 strated that, apart from correction for the errors in equatorial B_Z , the correction of R_C
 573 is also needed, and this latter correction requires the probes located close enough to the

Figure 12. (a) K_{cr} versus K_{min} gradient (blue error bars) and histogram of K_{min} gradient (red bars). (b) Histogram of the difference between the radial distance to the true IB and the point with $K_{min} = 8$.

574 current center (Liang et al., 2013). Such configurations are rather rare and were not avail-
 575 able for the majority of IBs in Dubyagin et al. (2018) and Haiducek et al. (2019b) stud-
 576 ies. At the same time, our Figure 9 demonstrates that the curvature radius in the IB vicin-
 577 ity undergoes strong variations during the course of the storm. This indicates that the
 578 R_C correction is more critical for the storm time than for the quiet period analyzed by
 579 Haiducek et al. (2019a).

580 In order to estimate the sensitivity of the K_{IB} estimation to the mapping error,
 581 we show K_{cr} versus the K_{min} radial gradient in Figure 12a. The blue error bars show
 582 the range between lower and upper estimates of K_{cr} . There is no clear dependence of
 583 K_{cr} on $\partial K_{min}/\partial r$. Note however that three lowest K_{cr} values correspond to the weak
 584 gradient of $\sim -1R_E^{-1}$. It is rather surprising because Figures 1 and 8 clearly demonstrate
 585 that lowest K_{cr} values can be found during the peak of the storm in the near-Earth re-
 586 gion where the radial gradients are supposed to be strong. The histogram of K_{min} ra-
 587 dial gradient is shown by red. It can be seen that for the majority of IBs, the absolute
 588 value of the gradient is in the range of 1–8 R_E^{-1} with the most probable value of ~ 4 –
 589 5. Thus, if one assumes that the error of the mapping is $1R_E$, then the corresponding
 590 error of the K_{min} estimate is between 1 and 8. In other words, under such assumption,
 591 the mapping error can explain $K_{IB} \sim 15$, but it is unlikely that it will lead to higher
 592 values of K_{IB} estimates. Note that IBs with $K_{IB} > 15$ comprise a prominent share (\sim
 593 20–30%) of the statistical distributions found in Dubyagin et al. (2018) and Haiducek
 594 et al. (2019b). On the other hand, the mapping error obviously depends on the config-
 595 uration and is higher in the current sheet-like region. Therefore the aforementioned ar-
 596 guments should be considered with caution. Note also, that Figure 9 shows that the loss
 597 cone filling occurs in higher B_{eq} region during the peak of the storm and this might partly
 598 compensate the mapping error related to worse performance of magnetic field models
 599 during these dynamic periods.

600 It can be clearly seen in Figure 8 that on the duskside the K_{cr} values are lower dur-
 601 ing the main phase and higher during the pre-storm and recovery intervals. In Section 5
 602 we have shown that it is due to larger size of the equatorial loss cone size at the IB lo-
 603 cation during the main phase. As a result, stronger scattering is required to fill the loss
 604 cone and the filling occurs at lower K_{cr} values. In turn, the larger loss cone size is due
 605 to larger equatorial magnetic field magnitude and this reflects specific properties of the
 606 main phase magnetic configuration: the same values of K_{min} correspond to the higher
 607 values of magnetic field magnitude and lower values of R_C .

608 We confirm the result of Delcourt et al. (2000) that the presence of the guide (az-
 609 imuthal) component affects the strength of the pitch angle scattering and hence the K_{cr}
 610 values. It was found that the K_{cr} variation caused by B_φ in the SWMF simulation is
 611 comparable to that caused by the loss cone size variation. However, it should be noted
 612 that both effects, loss cone size and guide component variability, only cause K_{cr} vari-
 613 ation within narrow range of $K_{cr} = 4-8$ and these values are rather close to those ob-
 614 tained previously for simpler magnetic configurations (Tsyganenko, 1982; Sergeev et al.,
 615 1983; Delcourt et al., 1996). Since K_{cr} values of 8 is conventionally used to tie the low-
 616 altitude IB observations to the equatorial magnetosphere (Shevchenko et al., 2010), we
 617 evaluate the size of the error in terms of equatorial radial distance which can result from
 618 using this fixed value instead of true K_{cr} . In Figure 12b, we show the histogram of the
 619 difference in radial distance to the points with $K_{min} = 8$ and $K_{min} = K_{cr}$. It can be
 620 seen that for most of the cases the error is within $1 R_E$ and only on rare occasions it can
 621 be as large as 2 or 3 R_E .

622 7 Summary

623 To analyze the conditions of the loss cone filling by the scattering on the curved
 624 field lines during intense geomagnetic storm, we traced the trajectories of 30 keV pro-
 625 tons in the magnetic field of the SWMF simulation. The adiabaticity parameter (K_{cr})
 626 corresponding to the boundary between the empty and filled loss cone was determined
 627 for several nightside MLT sectors throughout the course of the storm. The results are
 628 summarized as follows:

- 629 1. No K_{cr} values greater than 8 have been found indicating that the extreme storm
 630 time magnetic configuration alone (not considering the electric field and non-stationary

631 effects) cannot cause the isotropic boundary formation at the K_{cr} values greater
632 than 8. The result suggests that higher K_{IB} values found in the observational stud-
633 ies for stationary periods, if not caused by the mapping error, should be attributed
634 to the wave-particle interaction.

- 635 2. The K_{cr} values tend to be lower (4–6) during the main phase and SYM-H min-
636 imum period.
- 637 3. This variation of K_{cr} is caused partly by variation of the equatorial loss cone size:
638 during the main phase, the K_{min} values typical for the isotropic boundary cor-
639 respond to much higher magnetic field, hence, stronger scattering is needed to fill
640 the larger equatorial loss cone size and its filling occurs at lower K_{min} values.
- 641 4. Another factor leading to variation of K_{cr} is the guide component of the magnetic
642 field (B_φ). It affects the strength of the pitch angle scattering and hence K_{cr} val-
643 ues. The effect is comparable quantitatively to that related to the loss cone size
644 variation.

645 **Acknowledgments**

646 The work leading to these results has been carried out in the Finnish Centre of Excel-
647 lence in Research of Sustainable Space (Academy of Finland grant numbers 312351, 312390),
648 which we gratefully acknowledge. The collaboration between Finnish Meteorological In-
649 stitute and St. Petersburg State University was supported by the Space Cooperation in
650 the Science and Technology Commission between Finland and Russia (TT/AVA), De-
651 cision No 331895 of the Academy of Finland. Work of NG was supported by NASA grants
652 #NNX17AI48G (ROSES 2016), #80NSSC20K0353 (ROSES 2018), and Heliophysics Phase I
653 DRIVE Science Center SOLSTICE (Solar Storms and Terrestrial Impacts Center) #80NSSC20K0600.
654 Work by EG and SA was supported by RFBR grant #19-05-00257. Simulation results
655 have been provided by the Community Coordinated Modeling Center at Goddard Space
656 Flight Center through their public Runs on Request system (<http://ccmc.gsfc.nasa.gov>).
657 The SWMF/BATS-R-US with RCM Model was developed by the T. Gombosi, R. Wolf,
658 S. Sazykin, G. Toth et al. at the Center for Space Environment Modelling, University
659 of Michigan, USA, and Department of Physics and Astronomy, Rice University, Texas,
660 USA.

References

- Asikainen, T., Maliniemi, V., & Mursula, K. (2010). Modeling the contributions of ring, tail, and magnetopause currents to the corrected Dst index. *Journal of Geophysical Research: Space Physics*, *115*(A12). Retrieved from <https://agupubs.onlinelibrary.wiley.com/doi/abs/10.1029/2010JA015774> doi: 10.1029/2010JA015774
- Baumjohann, W., & Treumann, R. (1996). *Basic space plasma physics* (Vol. 15-22). doi: 10.1142/p015
- Bock, R. K., & Krischer, W. (1998). *The data analysis briefbook* (1st ed.). Berlin, Heidelberg: Springer-Verlag.
- Büchner, J., & Zeleny, L. (1986). Deterministic chaos in the dynamics of charged particles near a magnetic field reversal. *Physics Letters A*, *118*(8), 395 - 399. Retrieved from <http://www.sciencedirect.com/science/article/pii/0375960186902689> doi: [https://doi.org/10.1016/0375-9601\(86\)90268-9](https://doi.org/10.1016/0375-9601(86)90268-9)
- Büchner, J., & Zelenyi, L. (1991). Regular and chaotic particle motion in sheared magnetic field reversals. *Advances in Space Research*, *11*(9), 177 - 182. Retrieved from <http://www.sciencedirect.com/science/article/pii/027311779190030N> doi: [https://doi.org/10.1016/0273-1177\(91\)90030-N](https://doi.org/10.1016/0273-1177(91)90030-N)
- Büchner, J., & Zelenyi, L. M. (1989). Regular and chaotic charged particle motion in magnetotail-like field reversals: 1. Basic theory of trapped motion. *Journal of Geophysical Research: Space Physics*, *94*(A9), 11821-11842. Retrieved from <https://agupubs.onlinelibrary.wiley.com/doi/abs/10.1029/JA094iA09p11821> doi: 10.1029/JA094iA09p11821
- Chen, H., Gao, X., Lu, Q., & Wang, S. (2019). Analyzing EMIC waves in the inner magnetosphere using long-term Van Allen probes observations. *Journal of Geophysical Research: Space Physics*, *124*(9), 7402-7412. Retrieved from <https://agupubs.onlinelibrary.wiley.com/doi/abs/10.1029/2019JA026965> doi: 10.1029/2019JA026965
- Delcourt, D. C., Malova, H. V., & Zelenyi, L. M. (2006). Quasi-adiabaticity in bifurcated current sheets. *Geophysical Research Letters*, *33*(6). Retrieved from <https://agupubs.onlinelibrary.wiley.com/doi/abs/10.1029/2005GL025463> doi: 10.1029/2005GL025463
- Delcourt, D. C., Sauvaud, J. A., Martin, R. F., & Moore, T. E. (1995). Gyrophase

- 694 effects in the centrifugal impulse model of particle motion in the magneto-
695 tail. *Journal of Geophysical Research: Space Physics*, 100(A9), 17211-17220.
696 Retrieved from [https://agupubs.onlinelibrary.wiley.com/doi/abs/](https://agupubs.onlinelibrary.wiley.com/doi/abs/10.1029/95JA00657)
697 10.1029/95JA00657 doi: 10.1029/95JA00657
- 698 Delcourt, D. C., Sauvaud, J.-A., Martin, R. F., & Moore, T. E. (1996). On the
699 nonadiabatic precipitation of ions from the near-Earth plasma sheet. *Journal*
700 *of Geophysical Research: Space Physics*, 101(A8), 17409-17418. Retrieved from
701 <https://agupubs.onlinelibrary.wiley.com/doi/abs/10.1029/96JA01006>
702 doi: 10.1029/96JA01006
- 703 Delcourt, D. C., Zelenyi, L. M., & Sauvaud, J.-A. (2000). Magnetic moment scat-
704 tering in a field reversal with nonzero BY component. *Journal of Geophysical*
705 *Research: Space Physics*, 105(A1), 349-359. Retrieved from [https://agupubs](https://agupubs.onlinelibrary.wiley.com/doi/abs/10.1029/1999JA900451)
706 [.onlinelibrary.wiley.com/doi/abs/10.1029/1999JA900451](https://agupubs.onlinelibrary.wiley.com/doi/abs/10.1029/1999JA900451) doi: 10.1029/
707 1999JA900451
- 708 Donovan, E. F., Jackel, B., Klumpar, D., & Strangeway, R. (2003). Energy depen-
709 dence of the isotropy boundary latitude. In *Proceedings of atmospheric studies*
710 *by optical methods* (Vol. 92, pp. 11–14). Sodankylä Geophysical Observatory
711 Publications.
- 712 Dubyagin, S., Ganushkina, N., Apatenkov, S., Kubyshkina, M., Singer, H., &
713 Liemohn, M. (2013). Geometry of duskside equatorial current during mag-
714 netic storm main phase as deduced from magnetospheric and low-altitude
715 observations. *Annales Geophysicae*, 31(3), 395–408. Retrieved from [https://](https://www.ann-geophys.net/31/395/2013/)
716 www.ann-geophys.net/31/395/2013/ doi: 10.5194/angeo-31-395-2013
- 717 Dubyagin, S., Ganushkina, N. Y., & Sergeev, V. (2018). Formation of 30 keV proton
718 isotropic boundaries during geomagnetic storms. *Journal of Geophysical Re-*
719 *search: Space Physics*, 123(5), 3436-3459. Retrieved from [https://agupubs](https://agupubs.onlinelibrary.wiley.com/doi/abs/10.1002/2017JA024587)
720 [.onlinelibrary.wiley.com/doi/abs/10.1002/2017JA024587](https://agupubs.onlinelibrary.wiley.com/doi/abs/10.1002/2017JA024587) doi: 10.1002/
721 2017JA024587
- 722 Erlandson, R. E., & Ukhorskiy, A. J. (2001). Observations of electromagnetic ion
723 cyclotron waves during geomagnetic storms: Wave occurrence and pitch angle
724 scattering. *Journal of Geophysical Research: Space Physics*, 106(A3), 3883-
725 3895. Retrieved from [https://agupubs.onlinelibrary.wiley.com/doi/abs/](https://agupubs.onlinelibrary.wiley.com/doi/abs/10.1029/2000JA000083)
726 [10.1029/2000JA000083](https://agupubs.onlinelibrary.wiley.com/doi/abs/10.1029/2000JA000083) doi: 10.1029/2000JA000083

- 727 Evans, D., & Greer, M. (2004, 01). Polar orbiting environmental satellite space envi-
728 ronment monitor - 2 instrument descriptions and archive data documentation.
729 *NOAA Tech. Memo. 1.4*.
- 730 Ganushkina, N. Y., Pulkkinen, T. I., Kubyshkina, M. V., Sergeev, V. A., Lvova,
731 E. A., Yahnina, T. A., ... Fritz, T. (2005). Proton isotropy boundaries as
732 measured on mid- and low-altitude satellites. *Annales Geophysicae*, 23, 1839–
733 1847. Retrieved from <https://www.ann-geophys.net/23/1839/2005/> doi:
734 10.5194/angeo-23-1839-2005
- 735 Gordeev, E., Sergeev, V., Honkonen, I., Kuznetsova, M., Rastätter, L., Palmroth,
736 M., ... Wiltberger, M. (2015). Assessing the performance of community-
737 available global mhd models using key system parameters and empirical
738 relationships. *Space Weather*, 13(12), 868-884. Retrieved from [https://](https://agupubs.onlinelibrary.wiley.com/doi/abs/10.1002/2015SW001307)
739 agupubs.onlinelibrary.wiley.com/doi/abs/10.1002/2015SW001307 doi:
740 10.1002/2015SW001307
- 741 Gvozdevsky, B. B., & Sergeev, V. A. (1996). MT-index – A possible new index to
742 characterize the configuration of the magnetotail. *Advances in Space Research*,
743 18(8), 51 - 54. Retrieved from [http://www.sciencedirect.com/science/](http://www.sciencedirect.com/science/article/pii/0273117795009957)
744 [article/pii/0273117795009957](http://www.sciencedirect.com/science/article/pii/0273117795009957) (The Three-dimensional Magnetosphere)
745 doi: [https://doi.org/10.1016/0273-1177\(95\)00995-7](https://doi.org/10.1016/0273-1177(95)00995-7)
- 746 Gvozdevsky, B. B., Sergeev, V. A., & Mursula, K. (1997). Long lasting energetic
747 proton precipitation in the inner magnetosphere after substorms. *Journal of*
748 *Geophysical Research: Space Physics*, 102(A11), 24333-24338. Retrieved from
749 <https://agupubs.onlinelibrary.wiley.com/doi/abs/10.1029/97JA02062>
750 doi: 10.1029/97JA02062
- 751 Haiducek, J. D., Ganushkina, N. Y., Dubyagin, S., & Welling, D. T. (2019a). On
752 the accuracy of adiabaticity parameter estimations using magnetospheric
753 models. *Journal of Geophysical Research: Space Physics*, 0(ja). Retrieved
754 from [https://agupubs.onlinelibrary.wiley.com/doi/abs/10.1029/](https://agupubs.onlinelibrary.wiley.com/doi/abs/10.1029/2018JA025916)
755 [2018JA025916](https://agupubs.onlinelibrary.wiley.com/doi/abs/10.1029/2018JA025916) doi: 10.1029/2018JA025916
- 756 Haiducek, J. D., Ganushkina, N. Y., Dubyagin, S., & Welling, D. T. (2019b). The
757 role of current sheet scattering in the proton isotropic boundary formation
758 during geomagnetic storms. *Journal of Geophysical Research: Space Physics*,
759 0(0). Retrieved from <https://agupubs.onlinelibrary.wiley.com/doi/abs/>

- 760 10.1029/2018JA026290 doi: 10.1029/2018JA026290
- 761 Halford, A. J., Fraser, B. J., & Morley, S. K. (2010). Emic wave activity dur-
762 ing geomagnetic storm and nonstorm periods: Crres results. *Journal of*
763 *Geophysical Research: Space Physics*, 115(A12). Retrieved from [https://](https://agupubs.onlinelibrary.wiley.com/doi/abs/10.1029/2010JA015716)
764 agupubs.onlinelibrary.wiley.com/doi/abs/10.1029/2010JA015716 doi:
765 10.1029/2010JA015716
- 766 Ilie, R., Ganushkina, N., Toth, G., Dubyagin, S., & Liemohn, M. W. (2015).
767 Testing the magnetotail configuration based on observations of low-altitude
768 isotropic boundaries during quiet times. *Journal of Geophysical Re-*
769 *search: Space Physics*, 120(12), 10,557–10,573. Retrieved from [https://](https://agupubs.onlinelibrary.wiley.com/doi/abs/10.1002/2015JA021858)
770 agupubs.onlinelibrary.wiley.com/doi/abs/10.1002/2015JA021858 doi:
771 10.1002/2015JA021858
- 772 Kaufmann, R. L., & Lu, C. (1993). Cross-tail current: Resonant orbits. *Journal of*
773 *Geophysical Research: Space Physics*, 98(A9), 15447-15465. Retrieved from
774 <https://agupubs.onlinelibrary.wiley.com/doi/abs/10.1029/93JA01464>
775 doi: 10.1029/93JA01464
- 776 Keika, K., Takahashi, K., Ukhorskiy, A. Y., & Miyoshi, Y. (2013). Global charac-
777 teristics of electromagnetic ion cyclotron waves: Occurrence rate and its storm
778 dependence. *Journal of Geophysical Research: Space Physics*, 118(7), 4135-
779 4150. Retrieved from [https://agupubs.onlinelibrary.wiley.com/doi/abs/](https://agupubs.onlinelibrary.wiley.com/doi/abs/10.1002/jgra.50385)
780 [10.1002/jgra.50385](https://agupubs.onlinelibrary.wiley.com/doi/abs/10.1002/jgra.50385) doi: 10.1002/jgra.50385
- 781 Kennel, C. F., & Petschek, H. E. (1966). Limit on stably trapped particle
782 fluxes. *Journal of Geophysical Research (1896-1977)*, 71(1), 1-28. Retrieved
783 from [https://agupubs.onlinelibrary.wiley.com/doi/abs/10.1029/](https://agupubs.onlinelibrary.wiley.com/doi/abs/10.1029/JZ071i001p00001)
784 [JZ071i001p00001](https://agupubs.onlinelibrary.wiley.com/doi/abs/10.1029/JZ071i001p00001) doi: 10.1029/JZ071i001p00001
- 785 Kubyshkina, M., Sergeev, V. A., Tsyganenko, N. A., & Zheng, Y. (2019). Testing ef-
786 ficiency of empirical, adaptive, and global MHD magnetospheric models to rep-
787 resent the geomagnetic field in a variety of conditions. *Space Weather*, 17(5),
788 672-686. Retrieved from [https://agupubs.onlinelibrary.wiley.com/doi/](https://agupubs.onlinelibrary.wiley.com/doi/abs/10.1029/2019SW002157)
789 [abs/10.1029/2019SW002157](https://agupubs.onlinelibrary.wiley.com/doi/abs/10.1029/2019SW002157) doi: 10.1029/2019SW002157
- 790 Kubyshkina, M. V., Sergeev, V. A., & Pulkkinen, T. I. (1999). Hybrid Input Al-
791 gorithm: An event-oriented magnetospheric model. *Journal of Geophysical*
792 *Research: Space Physics*, 104(A11), 24977-24993. Retrieved from [https://](https://agupubs.onlinelibrary.wiley.com/doi/abs/10.1029/1998JA000000)

- 793 agupubs.onlinelibrary.wiley.com/doi/abs/10.1029/1999JA900222 doi:
794 10.1029/1999JA900222
- 795 Larson, D. J., & Kaufmann, R. L. (1996). Structure of the magnetotail current
796 sheet. *Journal of Geophysical Research: Space Physics*, 101(A10), 21447-
797 21461. Retrieved from [https://agupubs.onlinelibrary.wiley.com/doi/
798 abs/10.1029/96JA01945](https://agupubs.onlinelibrary.wiley.com/doi/abs/10.1029/96JA01945) doi: 10.1029/96JA01945
- 799 Liang, J., Donovan, E., Ni, B., Yue, C., Jiang, F., & Angelopoulos, V. (2014).
800 On an energy-latitude dispersion pattern of ion precipitation potentially
801 associated with magnetospheric EMIC waves. *Journal of Geophysical Re-
802 search: Space Physics*, 119(10), 8137-8160. Retrieved from [https://
803 agupubs.onlinelibrary.wiley.com/doi/abs/10.1002/2014JA020226](https://agupubs.onlinelibrary.wiley.com/doi/abs/10.1002/2014JA020226) doi:
804 10.1002/2014JA020226
- 805 Liang, J., Donovan, E., Spanswick, E., & Angelopoulos, V. (2013). Multiprobe esti-
806 mation of field line curvature radius in the equatorial magnetosphere and the
807 use of proton precipitations in magnetosphere-ionosphere mapping. *Journal
808 of Geophysical Research: Space Physics*, 118(8), 4924-4945. Retrieved from
809 <https://agupubs.onlinelibrary.wiley.com/doi/abs/10.1002/jgra.50454>
810 doi: 10.1002/jgra.50454
- 811 Nishimura, Y., Shinbori, A., Ono, T., Iizima, M., & Kumamoto, A. (2006). Storm-
812 time electric field distribution in the inner magnetosphere. *Geophysical Re-
813 search Letters*, 33(22). Retrieved from [https://agupubs.onlinelibrary
814 .wiley.com/doi/abs/10.1029/2006GL027510](https://agupubs.onlinelibrary.wiley.com/doi/abs/10.1029/2006GL027510) doi: 10.1029/2006GL027510
- 815 Popova, T. A., Yahnin, A. G., Demekhov, A. G., & Chernyaeva, S. A. (2018). Gen-
816 eration of EMIC waves in the magnetosphere and precipitation of energetic
817 protons: Comparison of the data from THEMIS high earth orbiting satellites
818 and POES low earth orbiting satellites. *Geomagnetism and Aeronomy (Engl.
819 Transl.)*, 58(4), 469–482. doi: 10.1134/S0016793218040114
- 820 Rowland, D. E., & Wygant, J. R. (1998). Dependence of the large-scale, in-
821 ner magnetospheric electric field on geomagnetic activity. *Journal of Geo-
822 physical Research: Space Physics*, 103(A7), 14959–14964. Retrieved from
823 <https://agupubs.onlinelibrary.wiley.com/doi/abs/10.1029/97JA03524>
824 doi: 10.1029/97JA03524
- 825 Semenova, N. V., Yahnin, A. G., Yahnina, T. A., & Demekhov, A. G. (2019).

826 Properties of localized precipitation of energetic protons equatorward of the
827 isotropic boundary. *Geophysical Research Letters*, *46*(20), 10932-10940.
828 Retrieved from [https://agupubs.onlinelibrary.wiley.com/doi/abs/](https://agupubs.onlinelibrary.wiley.com/doi/abs/10.1029/2019GL085373)
829 [10.1029/2019GL085373](https://agupubs.onlinelibrary.wiley.com/doi/abs/10.1029/2019GL085373) doi: 10.1029/2019GL085373

830 Sergeev, V. A., Chernyaev, I. A., Angelopoulos, V., & Ganushkina, N. Y.
831 (2015). Magnetospheric conditions near the equatorial footpoints of pro-
832 ton isotropy boundaries. *Annales Geophysicae*, *33*(12), 1485–1493. Re-
833 trieved from <https://www.ann-geophys.net/33/1485/2015/> doi:
834 [10.5194/angeo-33-1485-2015](https://www.ann-geophys.net/33/1485/2015/)

835 Sergeev, V. A., Chernyaeva, S. A., Apatenkov, S. V., Ganushkina, N. Y., & Dubya-
836 gin, S. V. (2015). Energy-latitude dispersion patterns near the isotropy
837 boundaries of energetic protons. *Annales Geophysicae*, *33*(8), 1059–1070.
838 Retrieved from <https://www.ann-geophys.net/33/1059/2015/> doi:
839 [10.5194/angeo-33-1059-2015](https://www.ann-geophys.net/33/1059/2015/)

840 Sergeev, V. A., Malkov, M., & Mursula, K. (1993). Testing the isotropic bound-
841 ary algorithm method to evaluate the magnetic field configuration in the
842 tail. *Journal of Geophysical Research: Space Physics*, *98*(A5), 7609-7620.
843 Retrieved from [https://agupubs.onlinelibrary.wiley.com/doi/abs/](https://agupubs.onlinelibrary.wiley.com/doi/abs/10.1029/92JA02587)
844 [10.1029/92JA02587](https://agupubs.onlinelibrary.wiley.com/doi/abs/10.1029/92JA02587) doi: 10.1029/92JA02587

845 Sergeev, V. A., Sazhina, E. M., Tsyganenko, N. A., Lundblad, J. A., & Soraas, F.
846 (1983). Pitch-angle scattering of energetic protons in the magnetotail current
847 sheet as the dominant source of their isotropic precipitation into the nightside
848 ionosphere. *Planetary and Space Science*, *31*(10), 1147 - 1155. Retrieved from
849 <http://www.sciencedirect.com/science/article/pii/0032063383901034>
850 doi: [https://doi.org/10.1016/0032-0633\(83\)90103-4](https://doi.org/10.1016/0032-0633(83)90103-4)

851 Shevchenko, I. G., Sergeev, V., Kubyshkina, M., Angelopoulos, V., Glassmeier,
852 K. H., & Singer, H. J. (2010). Estimation of magnetosphere-ionosphere map-
853 ping accuracy using isotropy boundary and THEMIS observations. *Journal*
854 *of Geophysical Research: Space Physics*, *115*(A11). Retrieved from [https://](https://agupubs.onlinelibrary.wiley.com/doi/abs/10.1029/2010JA015354)
855 agupubs.onlinelibrary.wiley.com/doi/abs/10.1029/2010JA015354 doi:
856 [10.1029/2010JA015354](https://agupubs.onlinelibrary.wiley.com/doi/abs/10.1029/2010JA015354)

857 Speiser, T. W. (1965). Particle trajectories in model current sheets: 1. Analytical
858 solutions. *Journal of Geophysical Research*, *70*(17), 4219-4226. Retrieved

- 859 from <https://agupubs.onlinelibrary.wiley.com/doi/abs/10.1029/>
860 JZ070i017p04219 doi: 10.1029/JZ070i017p04219
- 861 Stephens, C. D., Brzozowski, R. W., & Jenko, F. (2017). On the limitations of
862 gyrokinetics: Magnetic moment conservation. *Physics of Plasmas*, *24*(10),
863 102517. Retrieved from <https://doi.org/10.1063/1.4998968> doi:
864 10.1063/1.4998968
- 865 Stern, D. P. (1966, Nov 01). The motion of magnetic field lines. *Space Science Re-*
866 *views*, *6*(2), 147–173. Retrieved from <https://doi.org/10.1007/BF00222592>
867 doi: 10.1007/BF00222592
- 868 Tsyganenko, N. A. (1982). Pitch-angle scattering of energetic particles in the
869 current sheet of the magnetospheric tail and stationary distribution func-
870 tions. *Planetary and Space Science*, *30*(5), 433 - 437. Retrieved from
871 <http://www.sciencedirect.com/science/article/pii/0032063382900526>
872 doi: [https://doi.org/10.1016/0032-0633\(82\)90052-6](https://doi.org/10.1016/0032-0633(82)90052-6)
- 873 Tsyganenko, N. A., & Andreeva, V. A. (2017). A hybrid approach to empirical mag-
874 netosphere modeling. *Journal of Geophysical Research: Space Physics*, *122*(8),
875 8198-8213. Retrieved from [https://agupubs.onlinelibrary.wiley.com/](https://agupubs.onlinelibrary.wiley.com/doi/abs/10.1002/2017JA024359)
876 [doi/abs/10.1002/2017JA024359](https://doi.org/10.1002/2017JA024359) doi: 10.1002/2017JA024359
- 877 Tsyganenko, N. A., & Sitnov, M. I. (2005). Modeling the dynamics of the in-
878 ner magnetosphere during strong geomagnetic storms. *Journal of Geo-*
879 *physical Research: Space Physics*, *110*(A3). Retrieved from [https://](https://agupubs.onlinelibrary.wiley.com/doi/abs/10.1029/2004JA010798)
880 [agupubs.onlinelibrary.wiley.com/doi/abs/10.1029/2004JA010798](https://doi.org/10.1029/2004JA010798) doi:
881 10.1029/2004JA010798
- 882 Tsyganenko, N. A., & Sitnov, M. I. (2007). Magnetospheric configurations
883 from a high-resolution data-based magnetic field model. *Journal of Geo-*
884 *physical Research: Space Physics*, *112*(A6). Retrieved from [https://](https://agupubs.onlinelibrary.wiley.com/doi/abs/10.1029/2007JA012260)
885 [agupubs.onlinelibrary.wiley.com/doi/abs/10.1029/2007JA012260](https://doi.org/10.1029/2007JA012260) doi:
886 10.1029/2007JA012260
- 887 Tóth, G., Sokolov, I. V., Gombosi, T. I., Chesney, D. R., Clauer, C. R., De Zeeuw,
888 D. L., ... Kóta, J. (2005). Space Weather Modeling Framework: A new tool
889 for the space science community. *Journal of Geophysical Research: Space*
890 *Physics*, *110*(A12). Retrieved from [https://agupubs.onlinelibrary.wiley](https://agupubs.onlinelibrary.wiley.com/doi/abs/10.1029/2005JA011126)
891 [.com/doi/abs/10.1029/2005JA011126](https://doi.org/10.1029/2005JA011126) doi: 10.1029/2005JA011126

- 892 Usanova, M. E., Mann, I. R., Bortnik, J., Shao, L., & Angelopoulos, V. (2012).
893 THEMIS observations of electromagnetic ion cyclotron wave occurrence:
894 Dependence on AE, SYMH, and solar wind dynamic pressure. *Journal of*
895 *Geophysical Research: Space Physics*, 117(A10). Retrieved from [https://](https://agupubs.onlinelibrary.wiley.com/doi/abs/10.1029/2012JA018049)
896 agupubs.onlinelibrary.wiley.com/doi/abs/10.1029/2012JA018049 doi:
897 10.1029/2012JA018049
- 898 West, H. I., Buck, R. M., & Kivelson, M. G. (1978). On the configuration of the
899 magnetotail near midnight during quiet and weakly disturbed periods: Mag-
900 netic field modeling. *Journal of Geophysical Research: Space Physics*, 83(A8),
901 3819-3829. Retrieved from [https://agupubs.onlinelibrary.wiley.com/](https://agupubs.onlinelibrary.wiley.com/doi/abs/10.1029/JA083iA08p03819)
902 [doi/abs/10.1029/JA083iA08p03819](https://agupubs.onlinelibrary.wiley.com/doi/abs/10.1029/JA083iA08p03819) doi: 10.1029/JA083iA08p03819
- 903 Yahnin, A., & Yahnina, T. (2007). Energetic proton precipitation related to ion-
904 cyclotron waves. *Journal of Atmospheric and Solar-Terrestrial Physics*,
905 69(14), 1690 - 1706. Retrieved from [http://www.sciencedirect.com/](http://www.sciencedirect.com/science/article/pii/S1364682607001885)
906 [science/article/pii/S1364682607001885](http://www.sciencedirect.com/science/article/pii/S1364682607001885) (Pc1 Pearl Waves: Discovery,
907 Morphology and Physics) doi: <https://doi.org/10.1016/j.jastp.2007.02.010>
- 908 Zhu, Z., & Parks, G. (1993). Particle orbits in model current sheets with a nonzero
909 by component. *Journal of Geophysical Research: Space Physics*, 98(A5), 7603-
910 7608. Retrieved from [https://agupubs.onlinelibrary.wiley.com/doi/abs/](https://agupubs.onlinelibrary.wiley.com/doi/abs/10.1029/92JA02366)
911 [10.1029/92JA02366](https://agupubs.onlinelibrary.wiley.com/doi/abs/10.1029/92JA02366) doi: 10.1029/92JA02366

Figure 1.

Author Manuscript

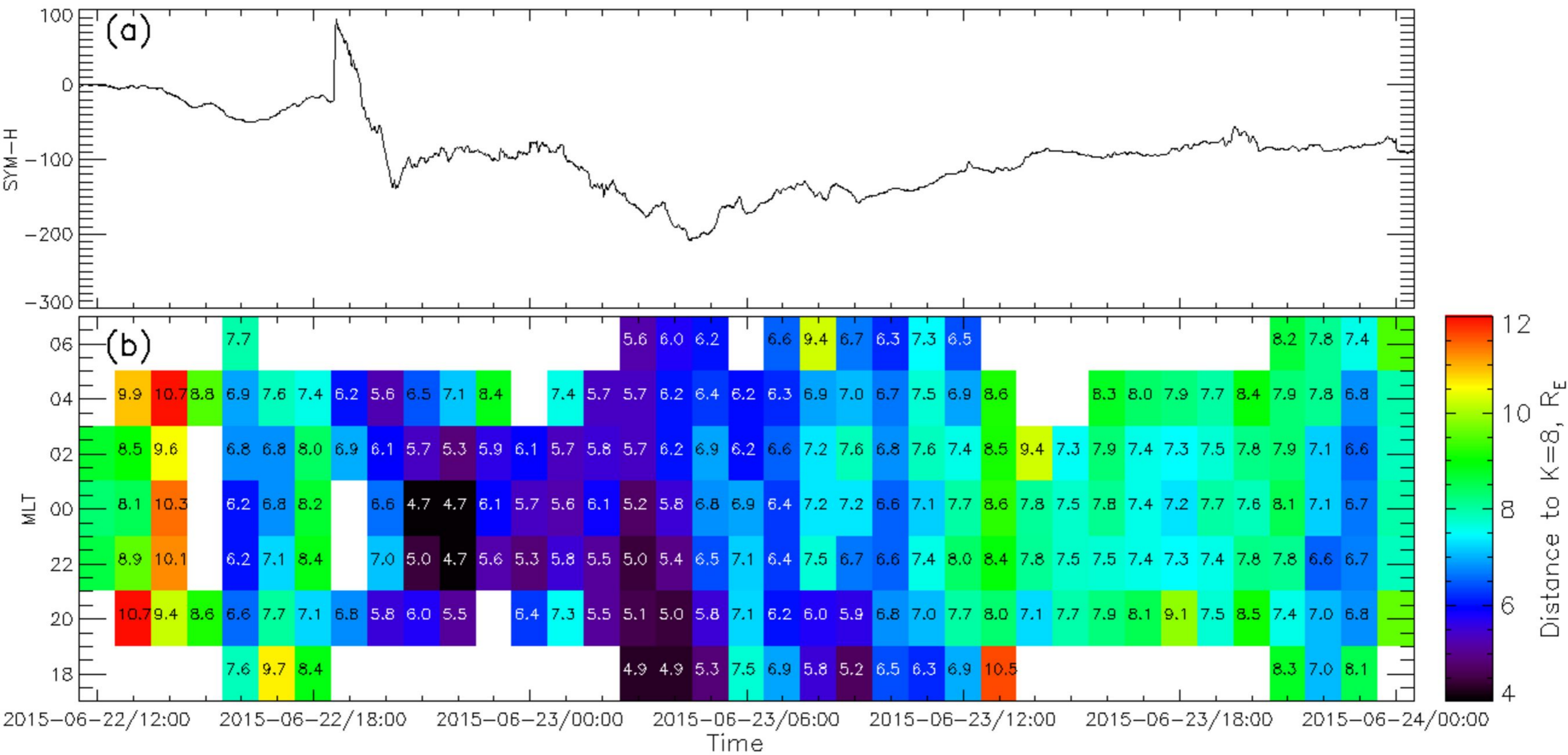
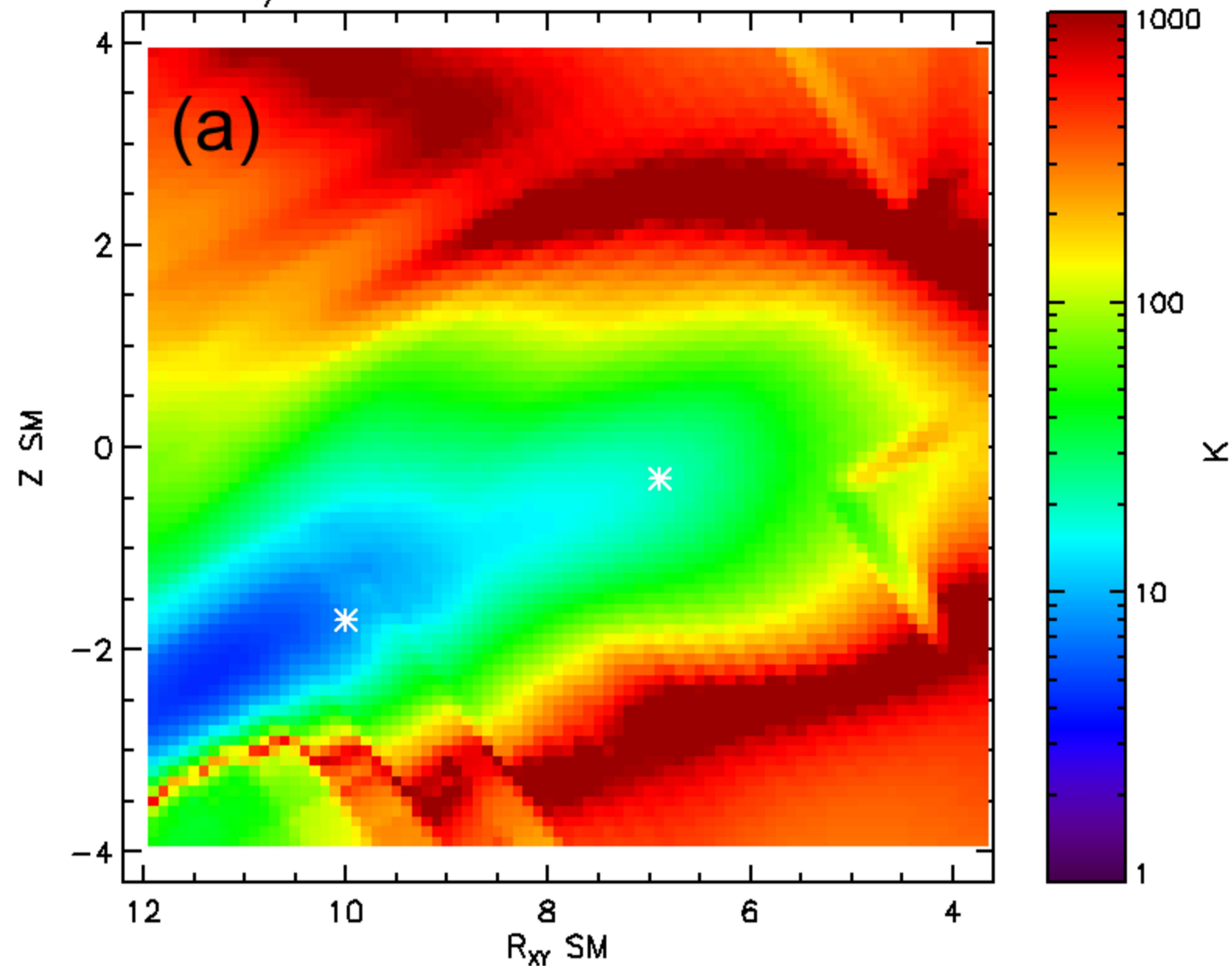


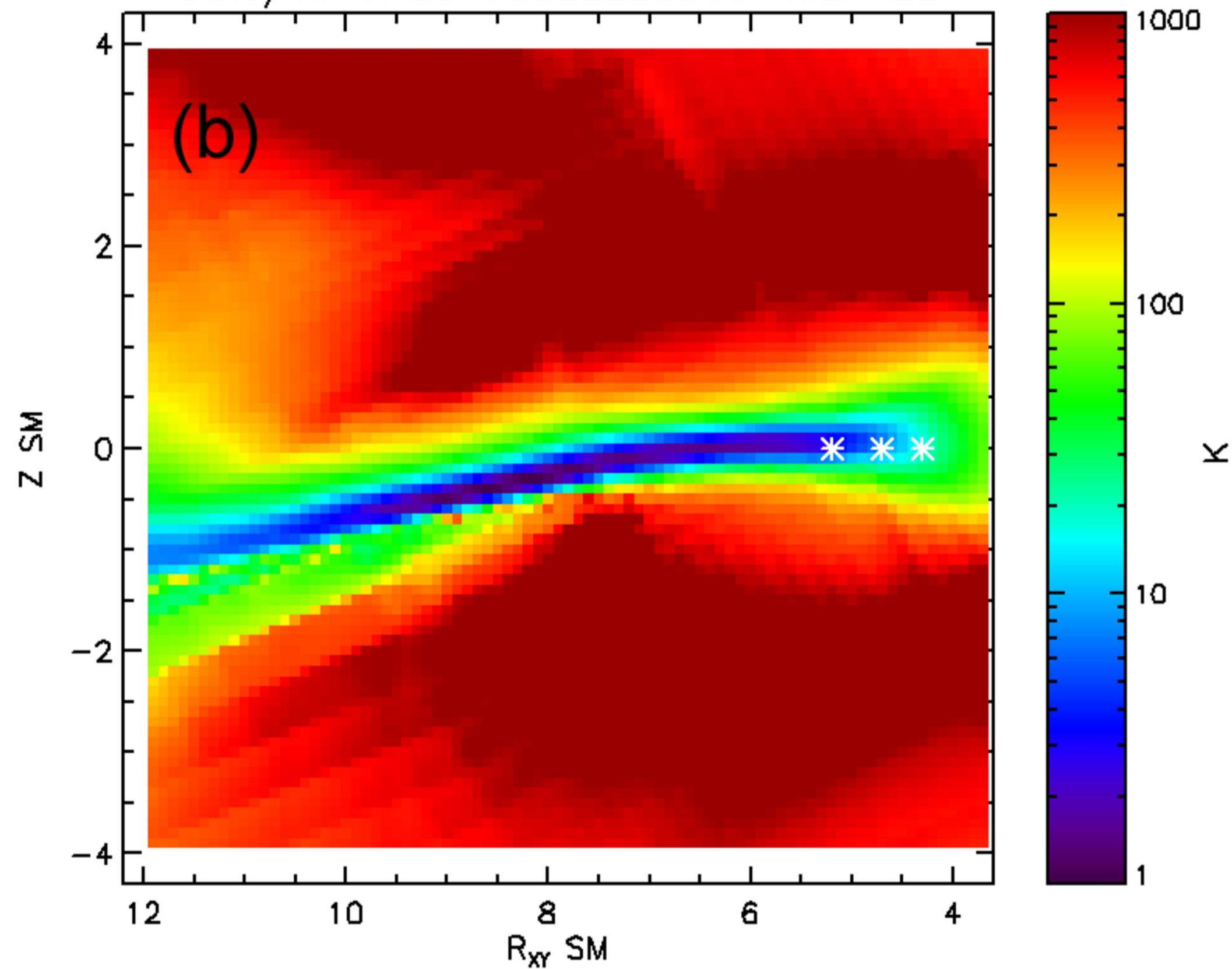
Figure 2.

Author Manuscript

Date/Time: 20150622140000 MLT=22



Date/Time: 20150622220000 MLT=22



Date/Time: 20150623130000 MLT=00

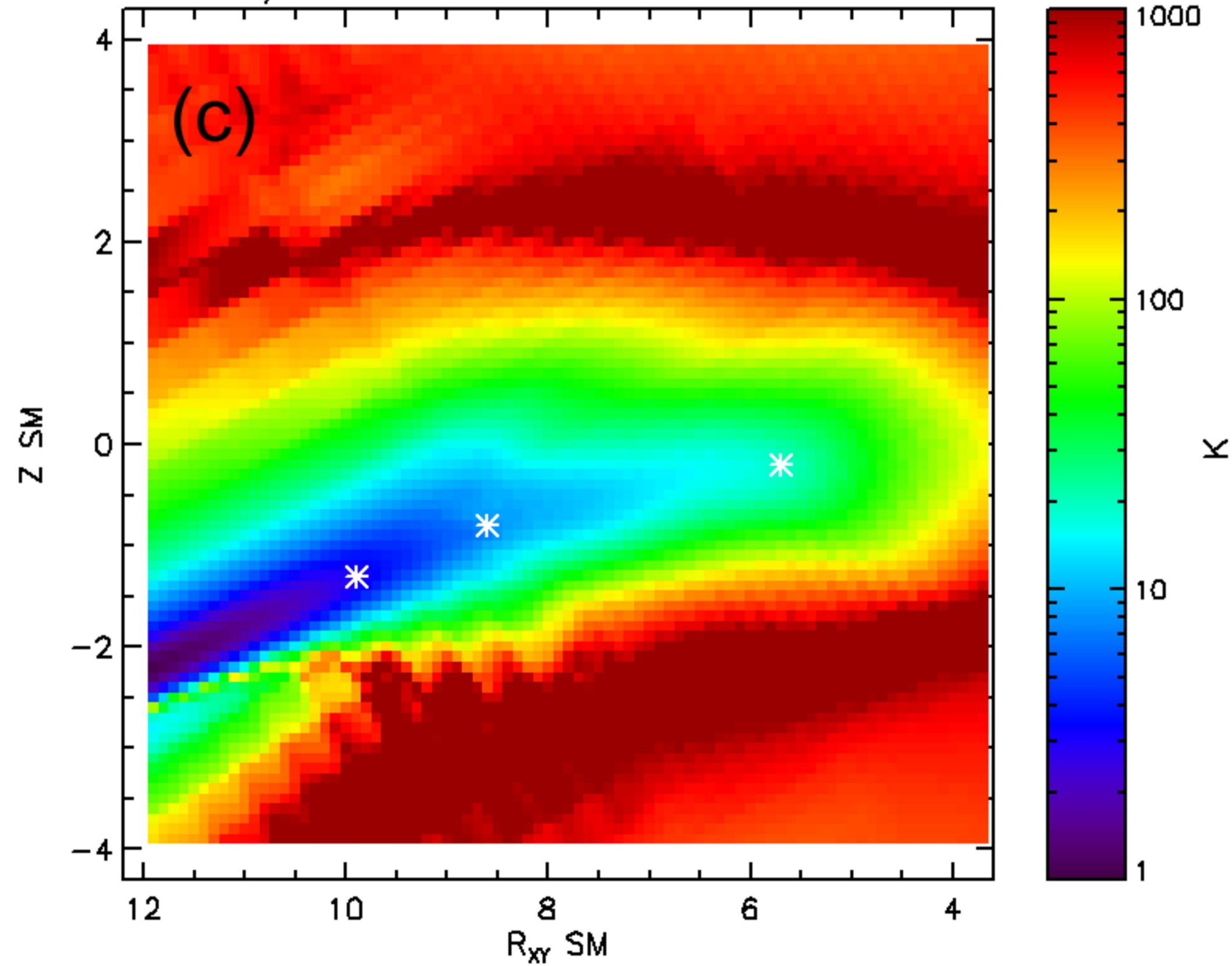


Figure 3.

Author Manuscript

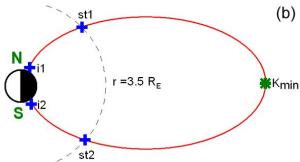
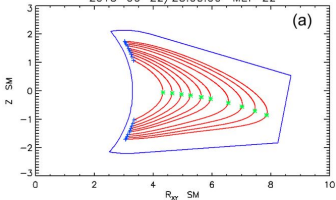
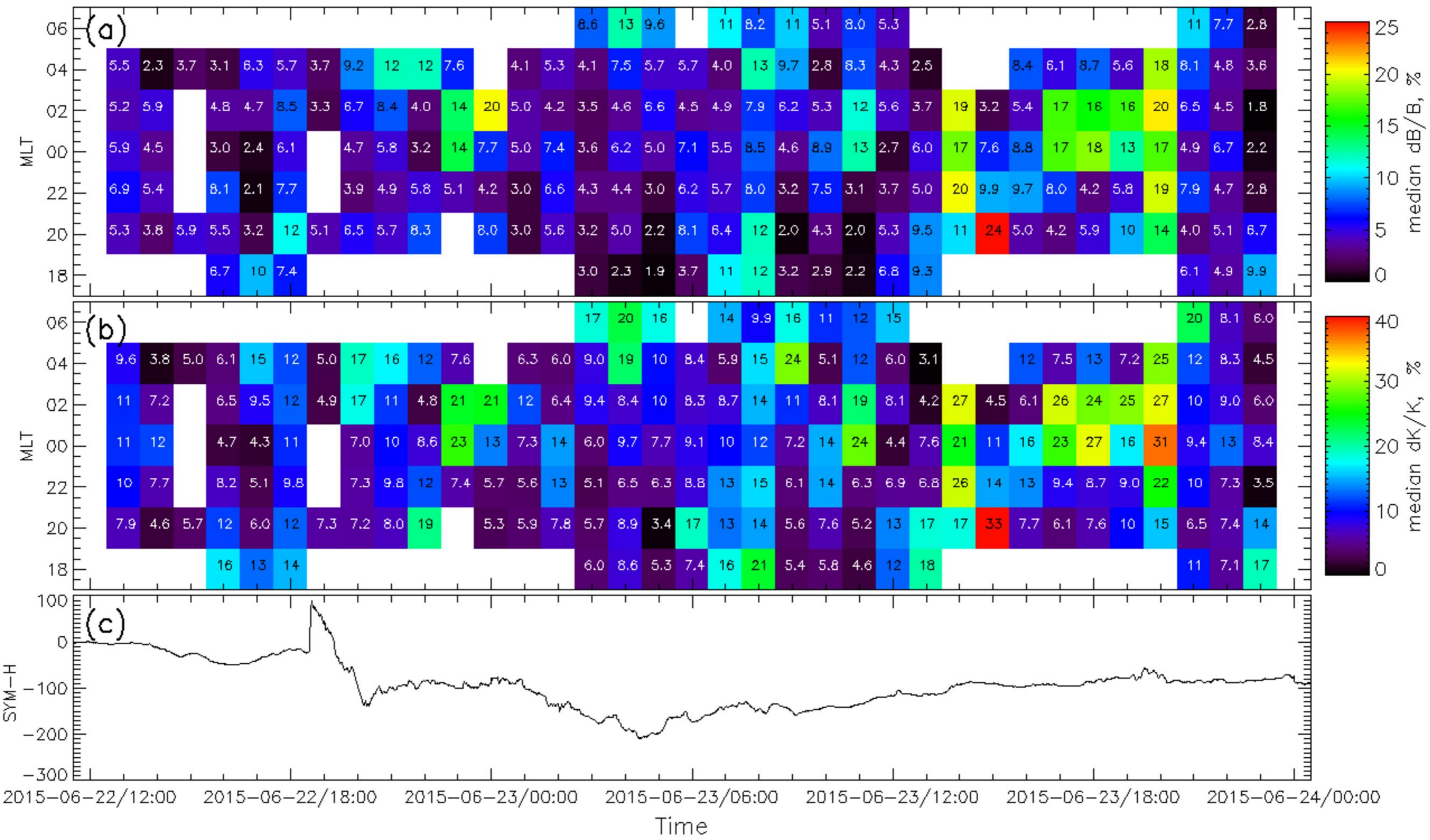


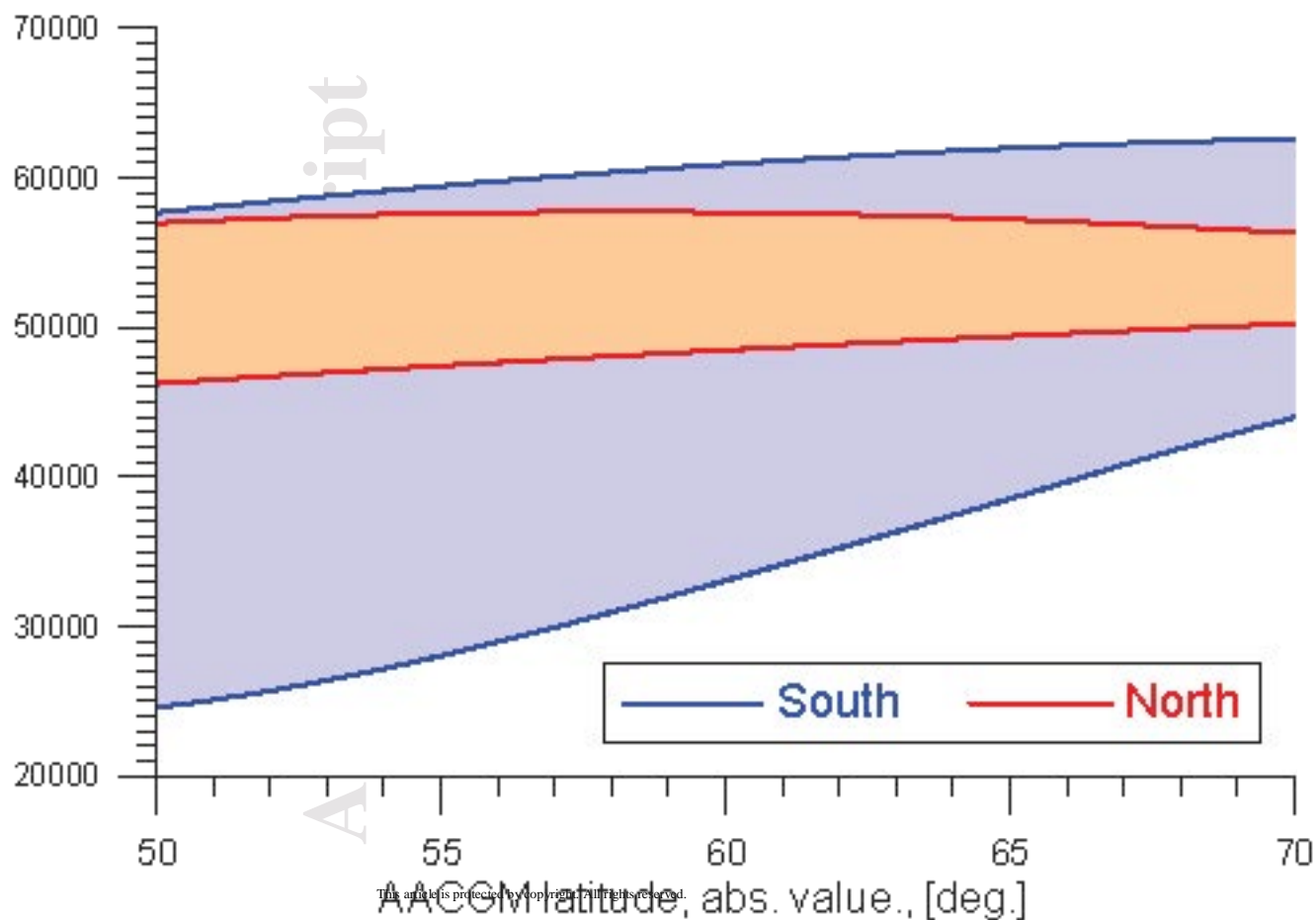
Figure 4.

Author Manuscript



Author Manuscript

Magnetic field at 120 km altitude

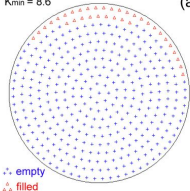


Author Manuscript

2015-06-22/22:00:00 MLT=22

$K_{\min} = 8.6$

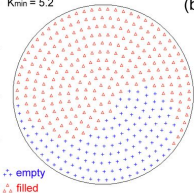
(a)



2015-06-22/22:00:00 MLT=22

$K_{\min} = 5.2$

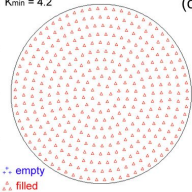
(b)



2015-06-22/22:00:00 MLT=22

$K_{\min} = 4.2$

(c)



Author Manuscript

2015-06-22/22:00:00 MLT=22

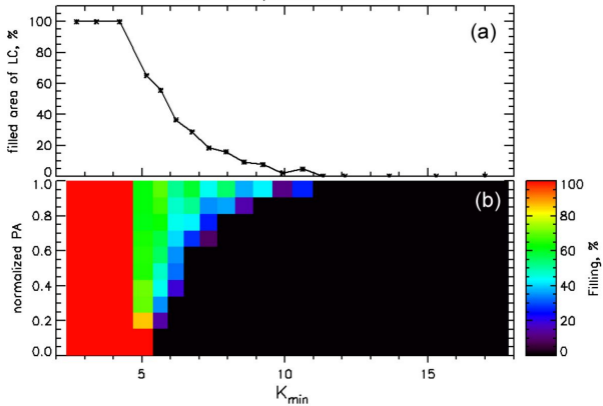
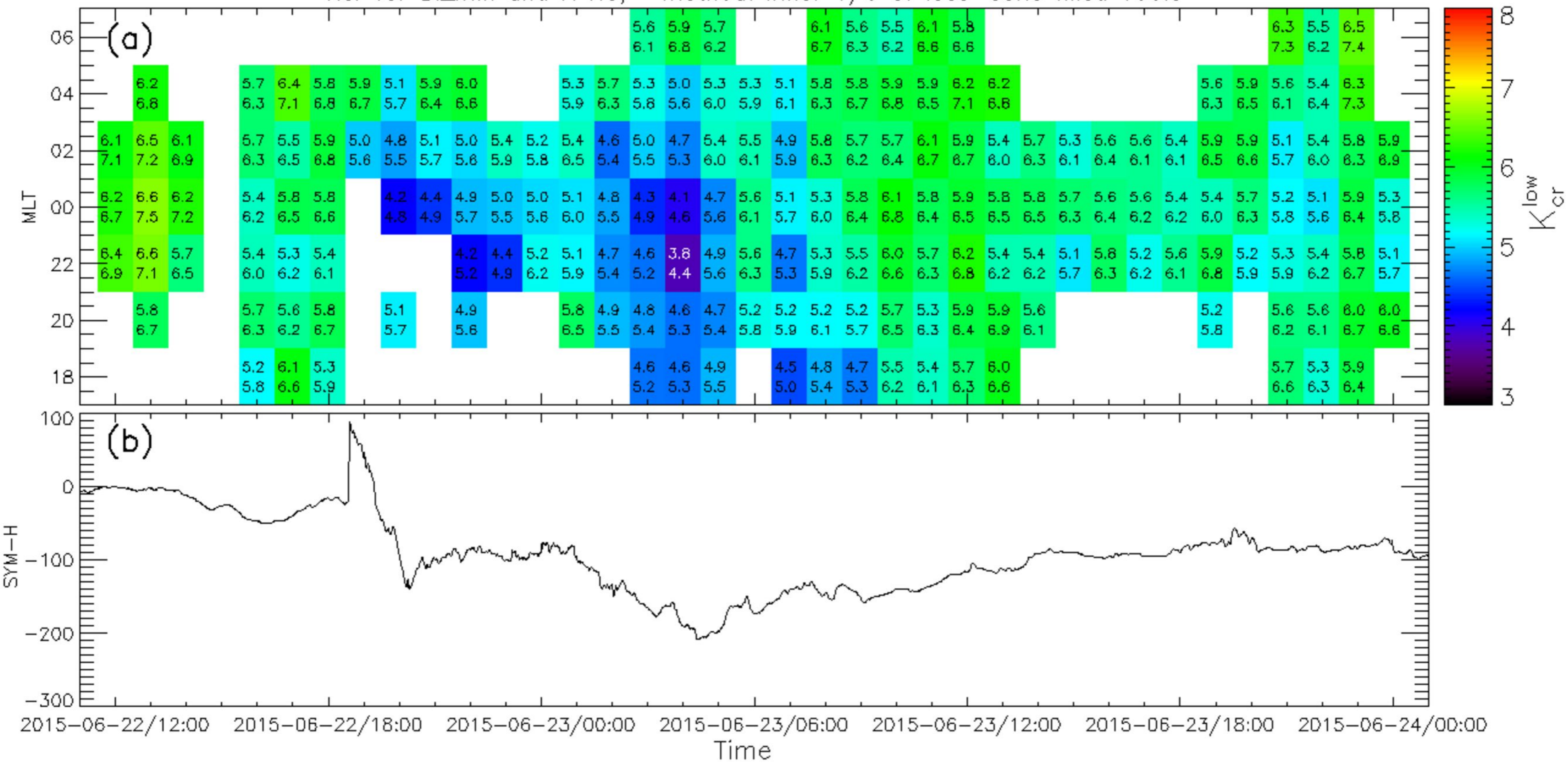


Figure 8.

Author Manuscript

Kcr for Bi_min and N HS, method: Inner 1/3 of loss-cone filled 100%



Author Manuscript

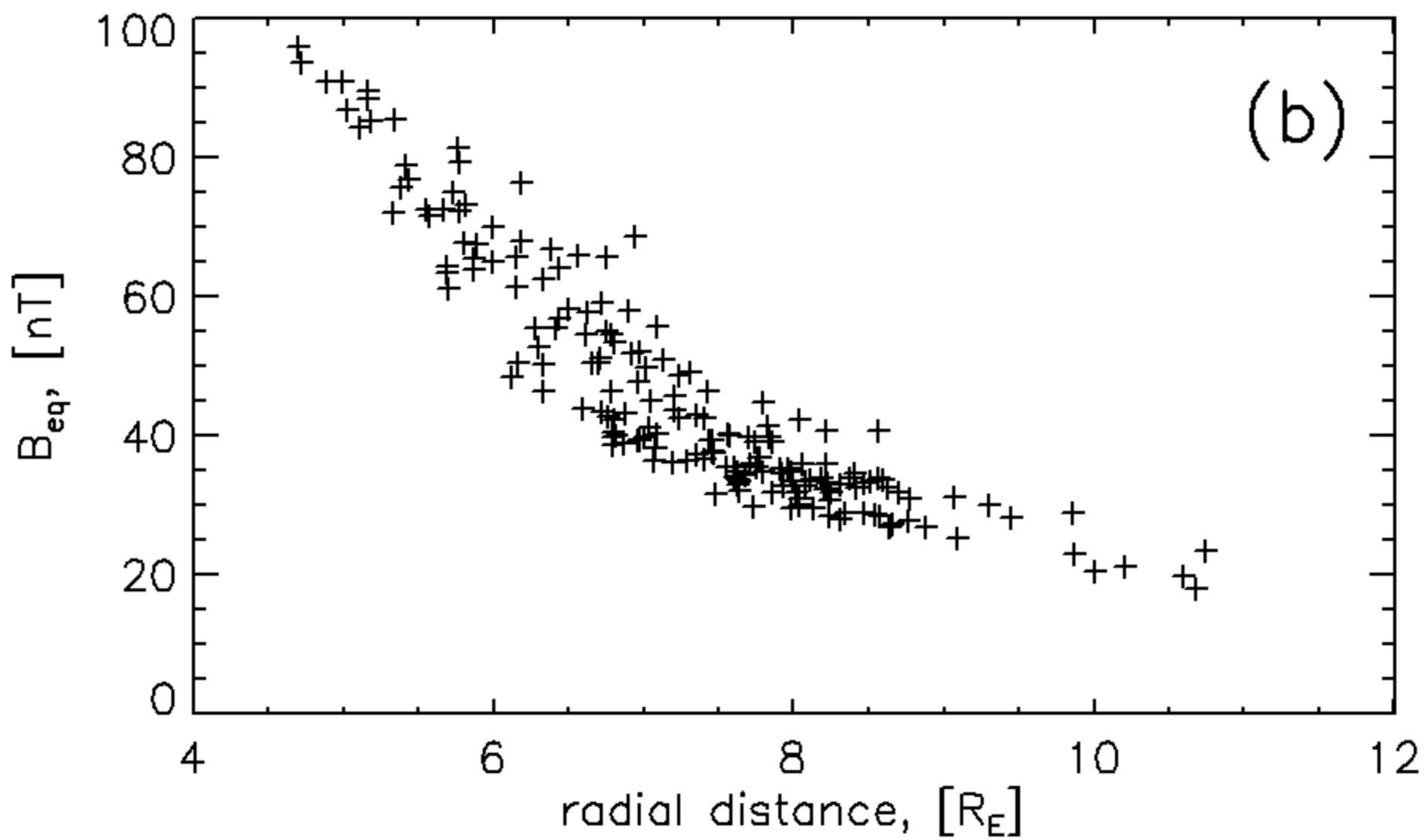
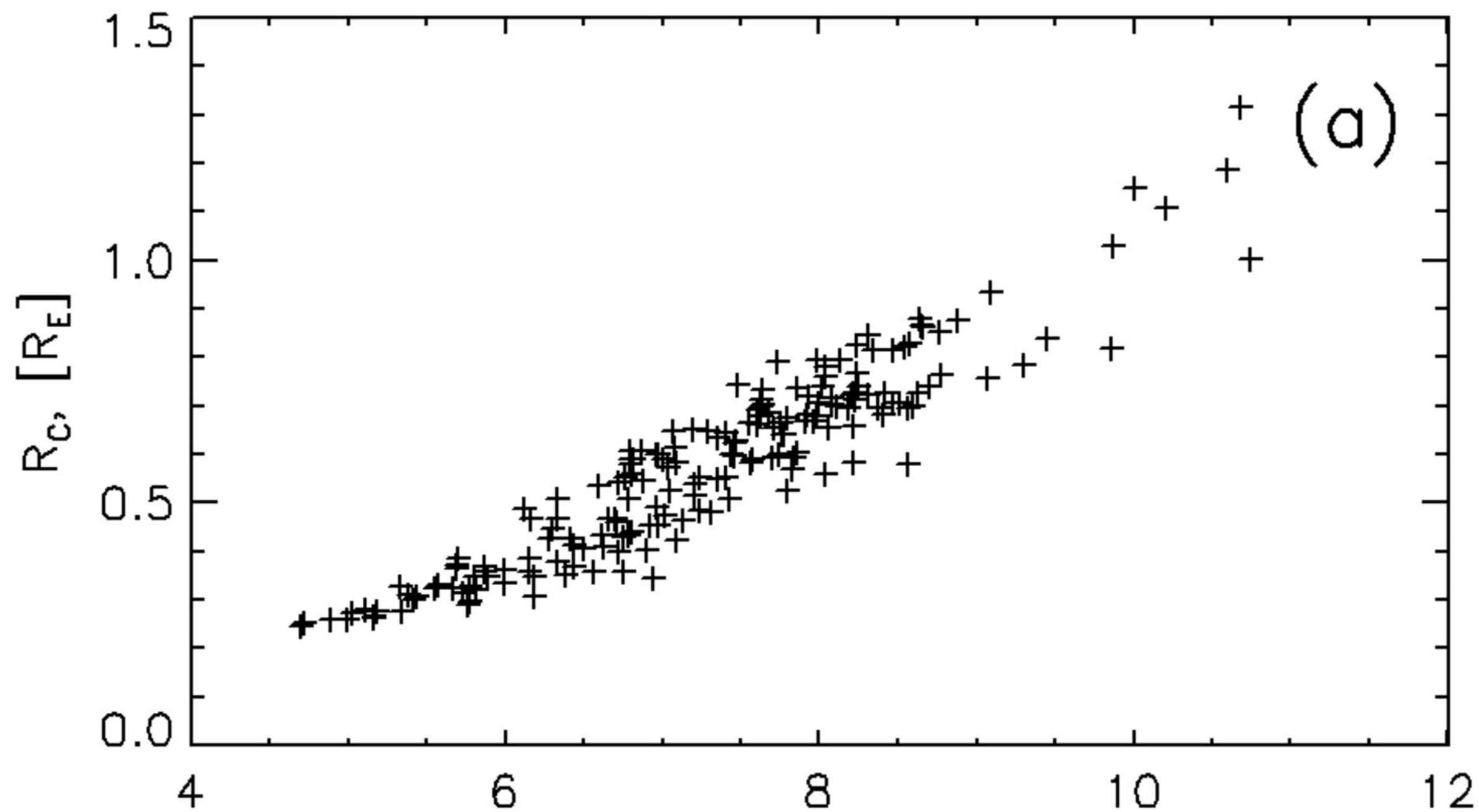
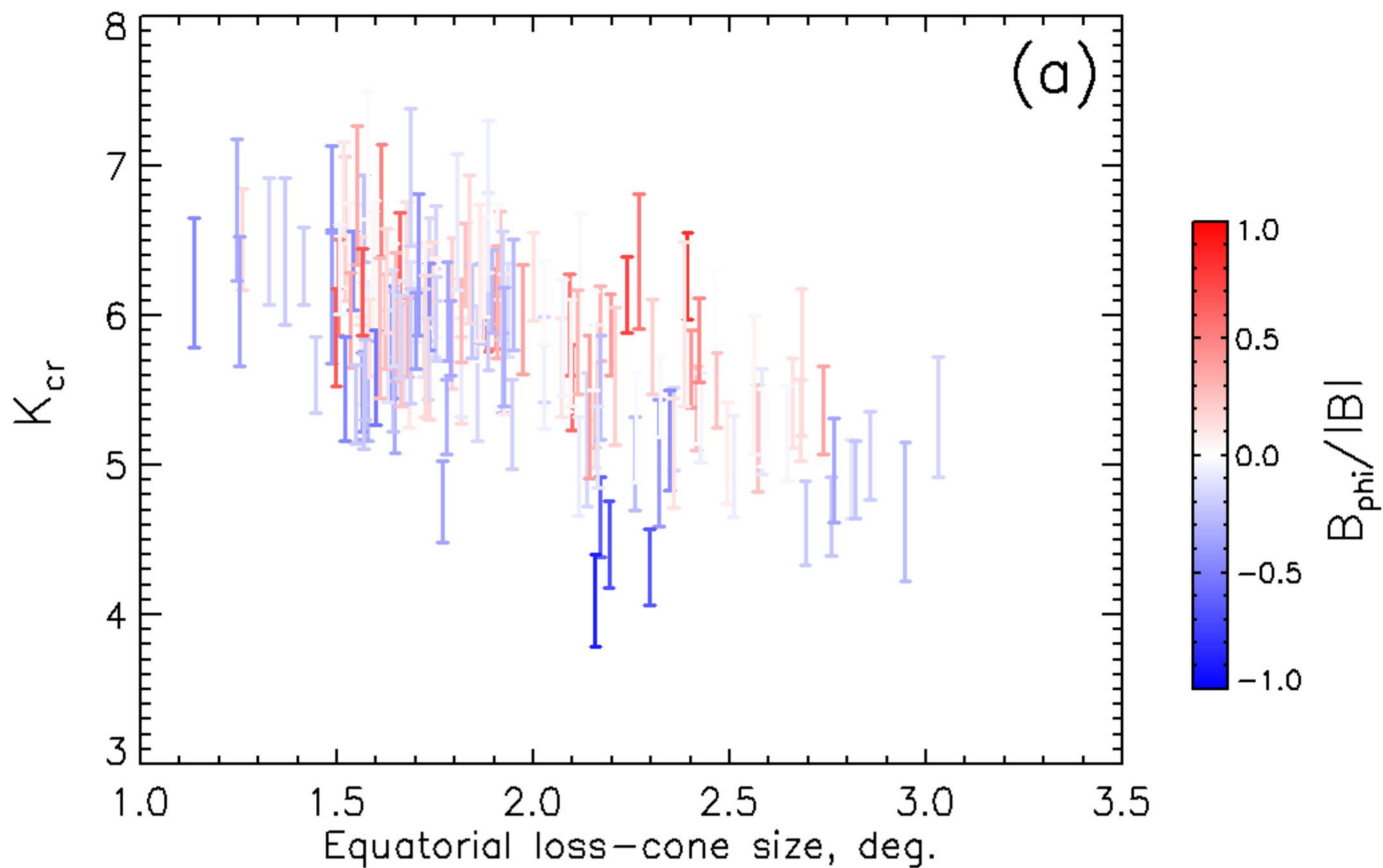


Figure 10.

Author Manuscript

Bi_min N HS



Bi_min S HS

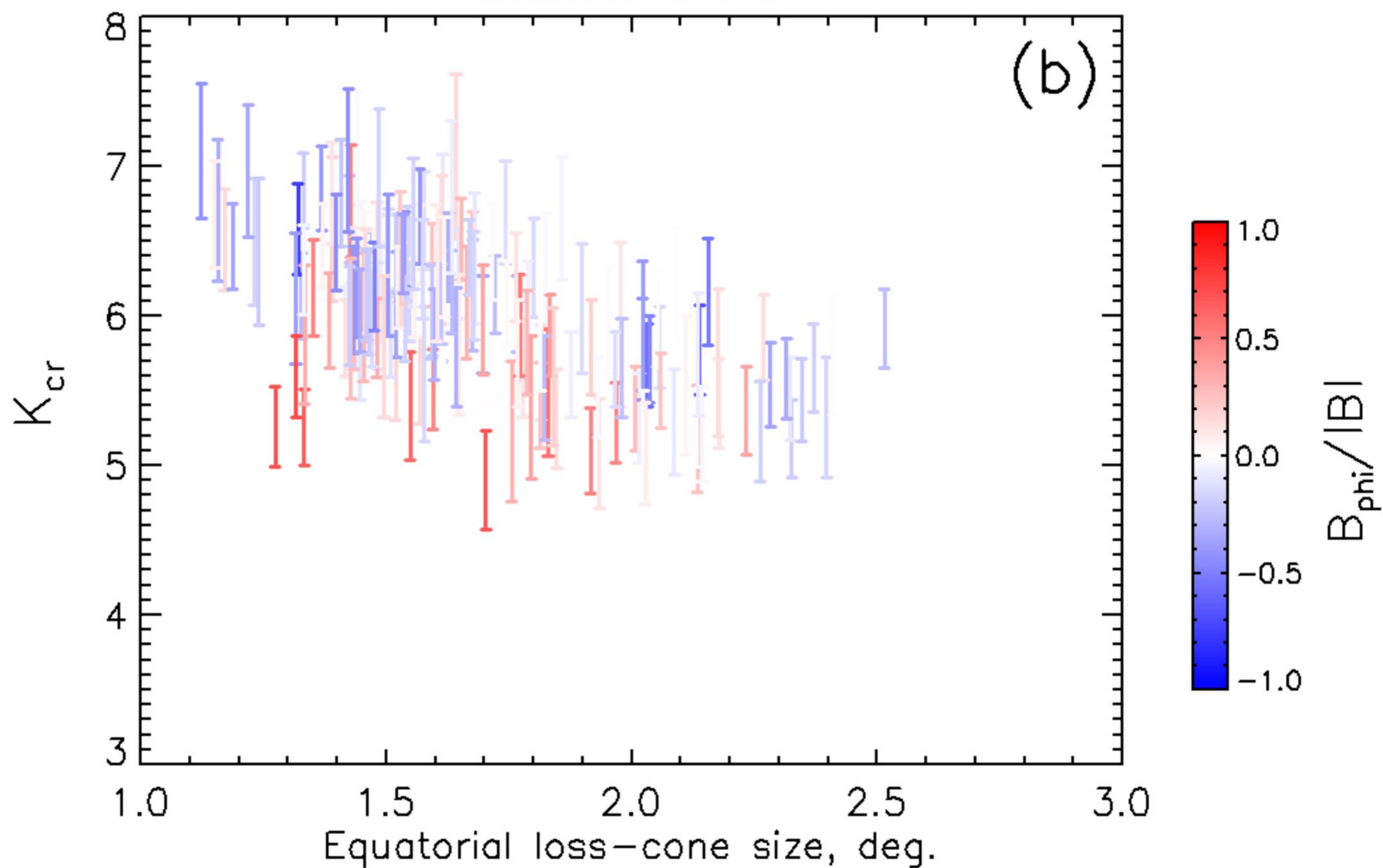
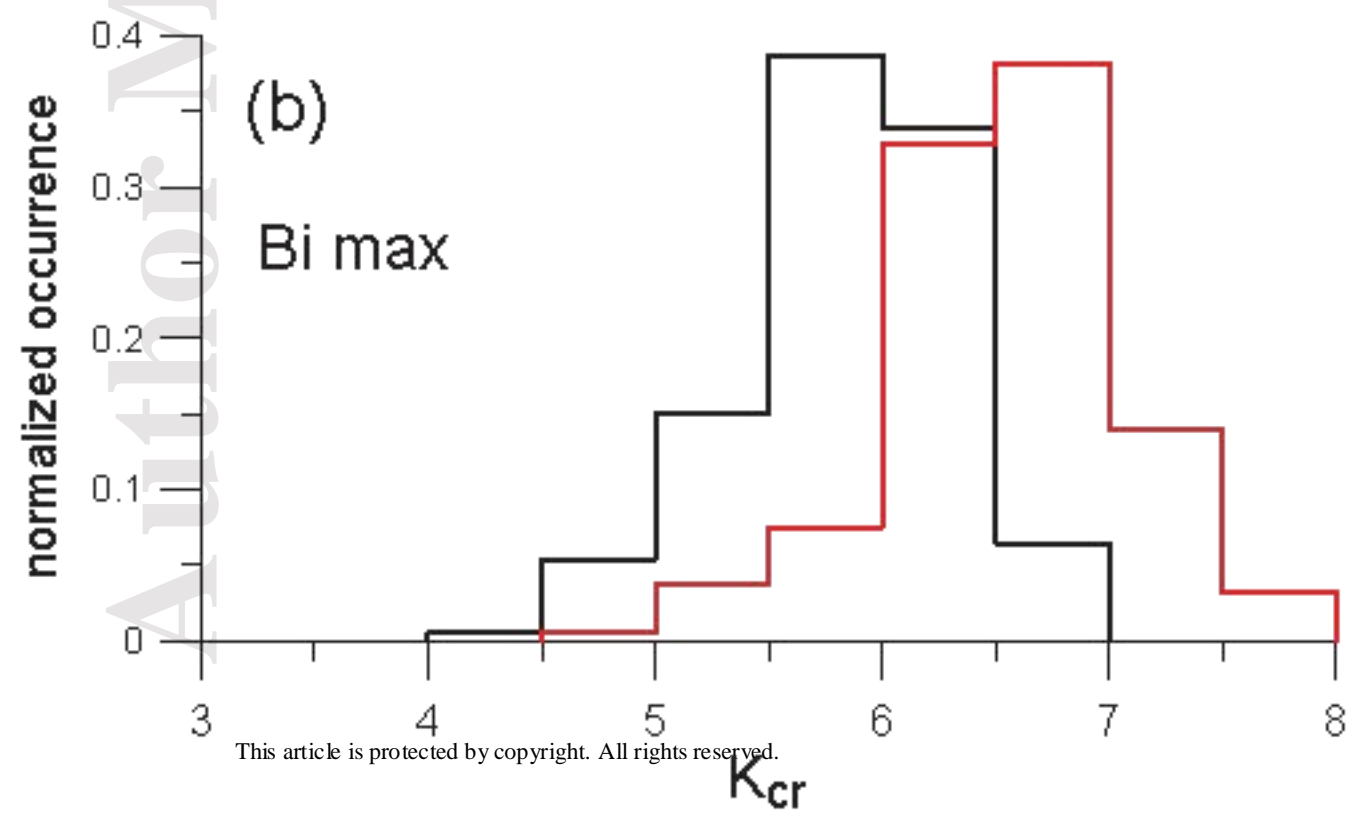
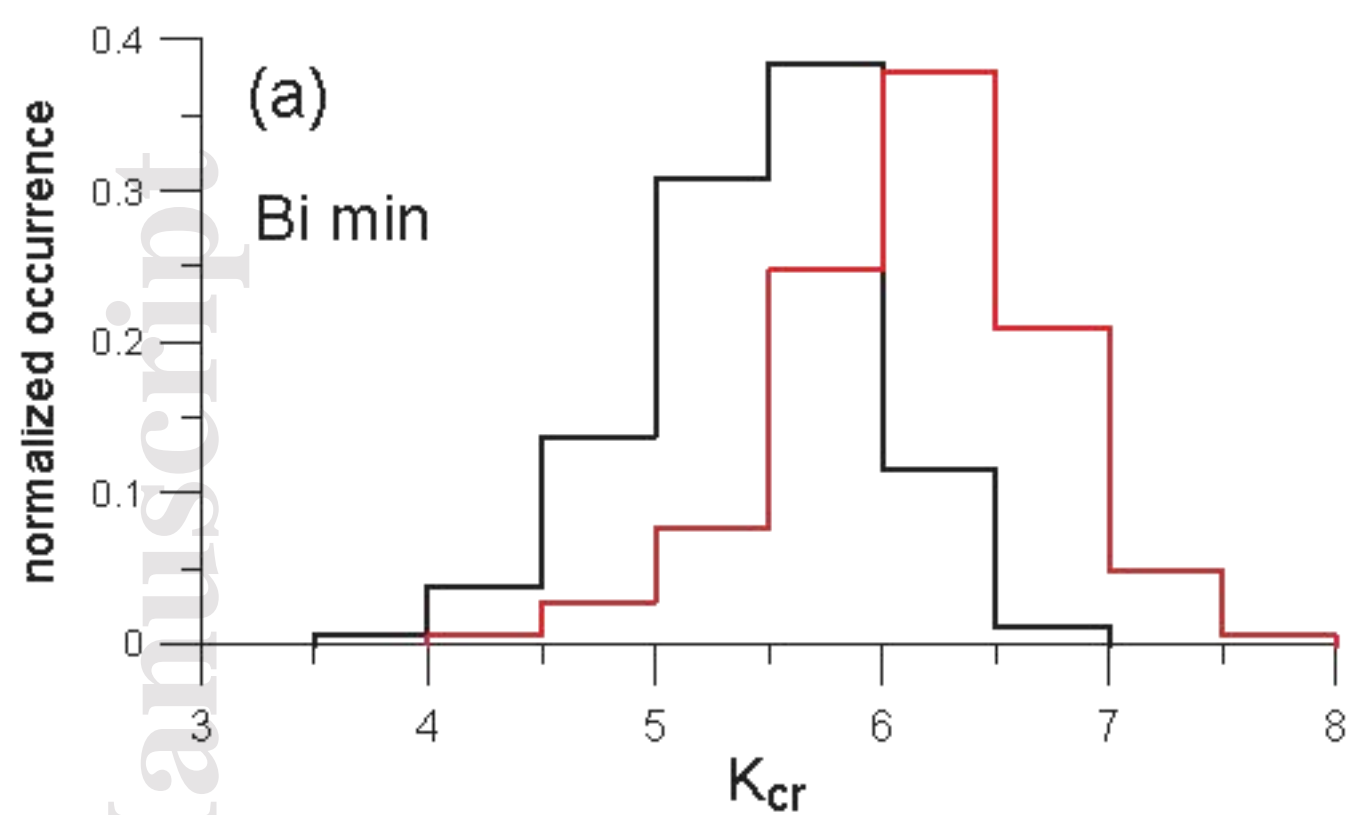


Figure 11.

Author Manuscript



Author Manuscript

